Tectonophysics 929 (2026) 231172

Contents lists available at ScienceDirect

Tectonophysics

journal homepage: www.elsevier.com/locate/tecto

Anatomy of a fluid-driven seismic swarm: The 2021–2023 Thiva earthquake sequence, central Greece

K.I. Konstantinou [a,*], V. Mouslopoulou [b], J. Begg [c]

[a] Department of Earth Sciences, National Central University, Jhongli, 320, Taiwan
[b] Institute of Geodynamics, National Observatory of Athens, PO Box 20048, 11810 Athens, Greece
[c] GNS Science, PO Box 30-368, Lower Hutt, New Zealand

ARTICLE INFO

Dataset link: http://eida.gein.noa.gr, https://bbnet.gein.noa.gr, https://www.generic-mapping-tools.org/, https://octave.org/, https://github.com/djpugh/MTplot

Keywords:
Seismicity
Moment tensor
Swarm
Fluids
Thiva
Greece

ABSTRACT

Earthquake swarms are associated with fluid movement along fracture zones and in some cases they have been found to precede large earthquakes. During 2021–2023 a swarm consisting of thousands of small and six moderate (Mw 3.9–4.3) events occurred in the area of Thiva in central Greece. We use seismological data recorded by 62 temporary and permanent stations along with geological observations to understand the swarm characteristics and its relationship with active faults. Precise earthquake locations indicate the activation of the Elaionas and Erythres-Dafnes fault systems, where seismicity was focused at depths 6–14 km in 2021 and 2022 respectively. Low values of effective stress drop (0.22–0.25 MPa) suggest that brittle asperities were embedded in a ductile rock matrix and this was probably one reason why the swarm was not followed by a larger earthquake. The temporal evolution of Vp/Vs shifts from 1.60–1.70 in 2021 to 1.36 during the early months of 2022 pointing to the possibility that a gaseous phase may have been involved. We also inverted P-wave polarities and SH/P amplitude ratios to determine 40 well-constrained moment tensor solutions. Most of these solutions indicate positive isotropic components with some of the events exhibiting shear-tensile faulting. The interaction of fluids with the rocks can progressively weaken faults in this area leading to a large earthquake. It is therefore of importance that the seismicity in Thiva is monitored continuously in order to realistically assess the seismic hazard.

1. Introduction

Earthquake swarms represent a facet of seismic activity where a sequence of earthquakes has no clearly identifiable mainshock. Swarms may occur naturally in volcanic areas due to magma intrusion (e.g., Passarelli et al., 2018; Lanza et al., 2022) or tectonic areas along active faults (Daniel et al., 2011; Yoshida and Hasegawa, 2018; Ross et al., 2020; Derode et al., 2023), but may also occur as a result of anthropogenic activities related to fluid injection (e.g., Keranen and Weingarten, 2018). It is widely accepted that the main cause of swarms is fluid movement through fracture zones and the subsequent reduction of frictional strength due to high pore pressure. Fluids may come from a variety of sources such as magma degassing (e.g., Santorini, Konstantinou et al., 2013; West Bohemia, Dahm and Fischer, 2014), slab dehydration (Mukuhira et al., 2023) or hydrological events in the form of heavy precipitation and snow melting (Hainzl et al., 2006; Shiddiqi et al., 2023). Aseismic slip processes were found to play an important role in the generation of swarm seismicity through stress transfer that can be induced by the fluid movement (Mouslopoulou et al., 2020; Danré et al., 2022). The study of swarms has attracted the attention of geoscientists as a way to better understand rock-fluid interactions and additionally for the reason that in some cases swarm activity is related to the preparation phase of large earthquakes. Examples where there is observational evidence for such a relationship include the earthquakes of 2009 (Mw 6.1) in L'Aquila, Italy (Cabrera et al., 2022), 2018 (Mw 6.9) in Zakynthos, Greece (Saltogianni et al., 2021), and 2024 (Mw 7.6) in Noto peninsula, Japan (Wang et al., 2024).

Greece and the Aegean Sea are regions that exhibit significant seismicity as a result of the subduction of the African slab beneath Eurasia and its subsequent rollback (Floyd et al., 2010; Fig. 1a). The regional stress field is dominated by N-S extension that changes orientation to E-W in the western and eastern margins of the subduction due to gravitational spreading (Konstantinou et al., 2017). The area of Thiva lies about 50 km NW from Athens, the capital of Greece, and is traversed by numerous normal faults orientated approximately E-W, some of which exhibit Holocene scarps (Fig. 1c, also see Konstantinou et al., 2020). Historical seismicity offers additional evidence for the recent activity of these faults with three earthquakes in 1853, 1893, 1914

* Corresponding author.
E-mail address: kkonst@ncu.edu.tw (K.I. Konstantinou).

https://doi.org/10.1016/j.tecto.2026.231172
Received 5 December 2025; Received in revised form 2 March 2026; Accepted 16 March 2026
Available online 17 March 2026
0040-1951/© 2026 Elsevier B.V. All rights reserved, including those for text and data mining, AI training, and similar technologies.

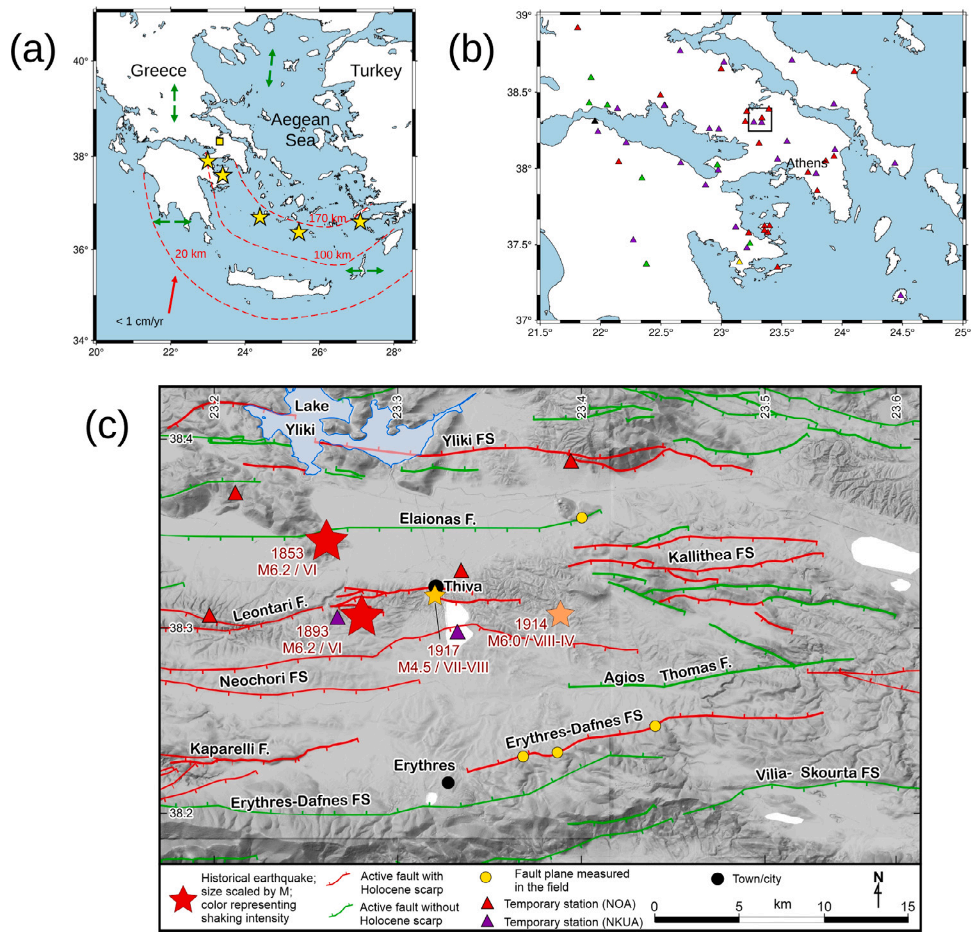

Fig. 1. (a) General tectonic setting in mainland Greece and the Aegean Sea. Red arrow shows the movement of the African Plate relative to Eurasia and double green arrows depict the orientation of extention based on regional stress (Konstantinou et al., 2017). The yellow stars represent the locations of active volcanoes. Dashed red lines are isodepths of intermediate depth seismicity adopted from Papazachos et al. (2000). The location of the area where the swarm occurred is shown as a square, (b) Map of the HUSN seismic stations utilized in this study. Red triangles are stations operated by NOAIG, purple triangles stations operated by the National Kapodistrian University of Athens, green triangles stations operated by the University of Patras, and yellow triangle station operated by the Aristotle University of Thessaloniki. The square indicates the area of Thiva and encloses the temporary stations installed in June 2021, (c) Digital Elevation Model (DEM) with overlain hillshade illustrating active and possibly active faults (from Begg et al., 2025) and the historical M > 6 seismicity in the study area. Ticks on active faults indicate down-faulted side. Field measurements are indicated by yellow circles and presented in Supporting Information Table S1.

that exhibited magnitudes between 6.0–6.2 and VI-VIII macroseismic intensities (Kaviris et al., 2022). It is interesting to note that according to Papazachos and Papazachou (2003), the 1893 event was preceded by an earthquake swarm that started in January 1892 and continued until May 1893 culminating in the occurrence of a M 6.2 earthquake. In June 2021 another swarm started in the area of Thiva that consisted of thousands of events (some of them with Mw 3.9–4.3) ending in 2023 without being followed by a large mainshock. Hence historic and modern observations indicate the potential of this area to produce long-duration swarms that may elevate the seismic hazard assessment not only for the vicinity of Thiva, but also for the broader metropolitan area of Athens (Konstantinou et al., 2020).

In this work, we make use of seismological data collected during and prior to the 2021–2023 Thiva swarm, coupled with geological observations, in order to understand the characteristics of the seismicity and its relationship with the active faults of the area. First, we describe the seismological data, in terms of permanent and temporary stations and, subsequently discuss the relationship of the recorded swarm with newly mapped faults in the area aided by field observations. Locations of events that have occurred from 2011 until 2023 are obtained in order to track the evolution from background to swarm seismicity and correlate earthquake locations with known active faults. The temporal variation of seismicity properties such as seismic moment release, effective stress drop, and b-value are also reconstructed in order to gain insights into the stress buildup and resulting deformation during the swarm. Another important parameter is the Vp/Vs ratio, whose temporal variation was also reconstructed providing clues about the nature of the fluid that was involved in the swarm. Full moment tensors were determined for earthquakes with $M_L \geq 2.8$ and give further evidence that the swarm caused not only shear but also tensile faulting. Finally, the discussion is divided into two parts: in the first part we put forward a plausible scenario that can explain the main characteristics of the swarm and their temporal occurrence in accordance with the geology of the Thiva area. The second part has to do with the implications of our findings in terms of seismic hazard, where we discuss whether a large earthquake is still possible in this area after the swarm.

2. Data

The seismic monitoring of mainland Greece and the Aegean area is accomplished through a dedicated network of permanent stations that form the Hellenic Unified Seismic Network (HUSN) (Fig. 1b). HUSN was formed after the merger of four individual seismic networks operated by the National Observatory of Athens, Institute of Geodynamics (hereafter referred to as NOAIG), and the Universities of Athens, Thessaloniki, and Patras. The network consists of more than 120 three-component seismic stations equipped with a variety of sensors (GMG-40T and CMG-3ESP, Trillium-120P, STS-2, Lennartz Le-3D-20s) recording at a sampling rate of 100 Hz. The continuous waveform recordings are relayed to NOAIG where the source parameters of each earthquake are first automatically determined and subsequently reviewed by the staff to ensure the reliability of the solution. Prior to the onset of the swarm in early June 2021, there was no seismic station installed in the vicinity of Thiva, and the closest station was about 20 km away. Within a few days after the onset of the swarm both NOAIG and the University of Athens installed six temporary broadband stations (THVA, THI1, THI2, THI3, THIV, AMPE) that were located 1–5 km away from the area where the bulk of the seismic activity was taking place (see Fig. 1b, c). As we will show later, the deployment of these stations improved significantly the accuracy of earthquake locations and provided valuable near-field observations for constraining Vp/Vs ratios as well as moment tensor solutions. In the subsequent analysis we make use of waveforms recorded by 6 temporary and another 56 permanent HUSN stations located within a maximum distance of 120 km from Thiva. This cutoff distance was determined after taking into account factors such as the signal-to-noise ratio of smaller events in the swarm, and the more complicated velocity structure at larger distances.

Active faults in the study area are adopted from Begg et al. (2025), a study undertaken partly by the authors of this study, during the evolution of the swarm. Begg et al. (2025) used high-resolution (2 m) Digital Elevation Models (DEMs) donated by the Greek Cadastre, together with published literature, to map (or remap) the geometry and extent of active surface fault traces proximal to Thiva. Although DEM analysis allows fault scarps > 1 m to be resolved, the stated fault lengths should be considered minima as traces that displace the ground surface by less than 1 meter could not be resolved (for more details see Begg et al., 2025). Nevertheless, our dataset samples all main faults in the area affected by the swarm (Fig. 1c). These faults are ground-truthed by Tsodoulos et al. (2008), Sboras et al. (2010), Konstantinou et al. (2020), Begg et al. (2025) and by the present study. In this context, we provide the main attributes in the Supporting Information Table S1. All active faults discussed are normal, with a general E-W strike and finite displacements ranging between 1 and 400 m (Fig. S1 in the Supplementary Information). The key normal faults involved in the Thiva swarm (the Elaionas Fault and the Erythres-Dafnes Fault System) form a small-scale tectonic graben, with secondary faults populating their hanging-wall (Fig. 1c).

3. Spatial distribution of seismicity

3.1. Earthquake relocation

For the purposes of this study we consider the seismicity that occurred in Thiva from early 2011 until the end of 2023. The year 2011 was chosen as the starting time of our analysis for the reason that by this point HUSN had been operating smoothly and it would be interesting to check the levels of background seismicity in Thiva prior to the swarm. Fig. 2 shows the distribution of seismicity based on the NOAIG catalog for the two time periods, namely from early 2011 up to May 2021, and from June 2021 up to the end of 2023. The period before the swarm exhibits low levels of seismicity with the rate of earthquakes most of the time not exceeding 5 events per 10 days, except from December 2, 2020 when a mainshock Mw 4.6 occurred and it was followed by about 120 aftershocks. Kaviris et al. (2022) have studied this earthquake sequence and have also performed Coulomb stress modeling in order to investigate its role as a trigger for the subsequent swarm. Their results indicate that static stress transfer due to the December 2020 mainshock is unlikely to have triggered the Thiva swarm which started six months later. The period during the swarm started with a sharp increase in earthquake rates with about 250 events that occurred during the first 10 days of June 2021.

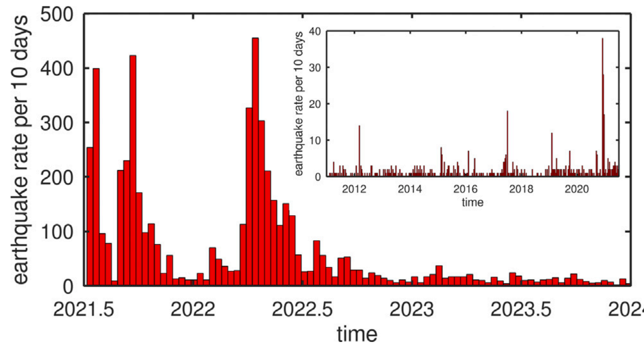

Fig. 2. Distribution of the number of earthquakes during the Thiva swarm using a bin size of 10 days. The inset in the upper right corner shows the distribution of earthquakes in the Thiva area from January 2011 until May 2021 using the same bin size. The large spike in the 2011–2021 distribution corresponds to the December 2, 2020 (Mw 4.6) mainshock and its aftershocks.

Three phases of activity can be seen during the swarm. The first phase corresponds to two bursts of seismicity in the summer months of 2021 followed by a progressive decrease of activity towards the end of the year. The second phase started with a gradual increase in the number of earthquakes during January and February 2022 with the largest increase in seismicity occurring in early March (~460 events in 10 days) and then gradually decaying activity up to August 2022. The final phase of seismic activity from August 2022 until the end of 2023 exhibited short duration (10–20 days) bursts of seismicity slowly decaying to background levels after the spring months of 2023. In total 522 events have been detected by NOAIG from 2011 until May 2021, while this number becomes 5523 events from June 2021 until December 2023.

We obtained absolute locations for a total of 6045 earthquakes contained in the NOAIG catalog using a nonlinear probabilistic algorithm implemented in the freely available software package NonLinLoc (Lomax et al., 2000). NonLinLoc offers complete sampling of the solution space using the Oct-Tree search algorithm making the location process more robust against local minima and also less influenced by outliers in the observed travel times. The P- and S-phase picks for all earthquakes were obtained from the NOAIG database, however, picks were adjusted manually whenever this was considered necessary. The velocity model used to calculate theoretical travel times is shown in Fig. 3 and it represents the minimum 1D model derived by Konstantinou et al. (2020) for the broader area around Athens (including the area of Thiva) using data from the permanent HUSN stations that are also utilized in this study. Earthquakes were first located using the minimum 1D velocity model and we utilized the average residual per station in order to calculate station corrections (Table S2 in supporting Information). The earthquakes were then located again, this time by applying the corrections, thus partly accounting for any travel time variations due to the 3D structure of the medium. Uncertainties were calculated for the final location of each event by using the diagonal elements of the covariance matrix provided by NonLinLoc (Maleki et al., 2013). We find that horizontal uncertainties have a mean of 0.92 km (±0.56 km), vertical uncertainties yield a mean value of 1.16 km (±0.87 km), while the rms residuals have a mean of 0.20 s (±0.06 s) (Fig. S2). A more careful look of the results reveals that the majority of events during 2011–2020 have vertical uncertainties that exceed 2.0 km, in contrast to most of the events during the swarm where uncertainties are less than 1.0 km both horizontal and vertically (Fig. S3). This difference can be easily explained by the fact that the 6 temporary stations installed in June 2021 provided numerous phases at small epicentral distances (1–5 km) improving significantly the quality of these locations. The final catalog of NonLinLoc locations along with their uncertainties is included as Table S3 in the Supporting Information.

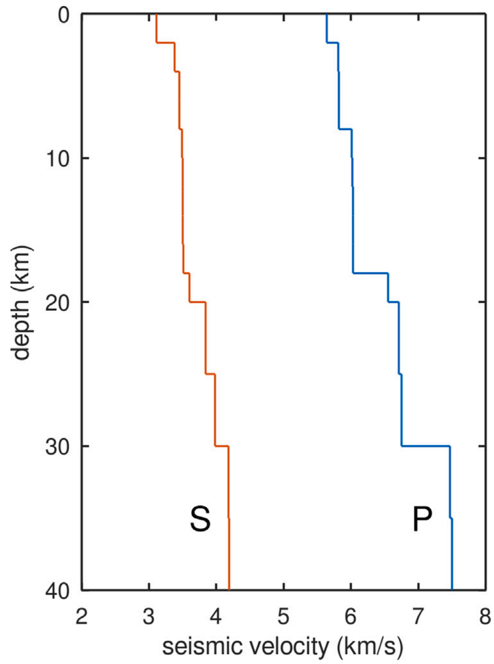

Fig. 3. Diagram depicting seismic velocities versus depth according to the minimum 1D velocity model derived by Konstantinou et al. (2020). Note that this model is well-constrained only for the top 20 km.

Absolute locations with horizontal and vertical uncertainties of 1.0 km or less were plotted on maps of the area along with focal mechanisms of the larger (Mw ≥ 4.0) events determined by NOAIG, superimposed on the main fault systems (Fig. 4). During 2011–2020 very few events could be found with small location uncertainties and most of them are aftershocks of the December 2020 main earthquake. In June 2021 events start clustering in the western part of the area and progressively migrate towards ESE. Three moderate (Mw 4.1–4.2) events occurred during this period that exhibited normal faulting but with slightly rotated nodal planes compared to the mainshock of December 2020 (Fig. 4b). In 2022 seismicity covers a larger area, expanding towards both east and west, while another three moderate (Mw 3.9–4.3) events occurred with faulting mechanisms similar to those in 2021. In 2023 the seismicity appears more scattered due to the smaller number of events, however, the areal extent is similar to the previous two years without showing any clear migration pattern. It is important to note that the long axis of the area delineated by the entire swarm aligns well with the strike of known faults at the surface, indicating that the seismicity is related to existing faults.

In order to understand better the relationship between the swarm seismicity and active faults we also plotted depth cross-sections for selected profiles where we include the topography along with the geometry of known faults and fault systems (Fig. 5). The seismicity forms two main clusters which are here interpreted to represent slip on fault planes of opposite dip: a steep plane (~67°) that dips towards SSE and another one, less steep (~56°) dipping towards NNW. The dip of these two clusters correlates very well with two active faults in the area, the Elaionas Fault (hereafter referred to as EF) and the Erythres-Dafnes Fault System (hereafter referred to as EDFS) respectively (Fig. 1c). In between these two faults there are numerous traces of other faults that likely extend to greater depths, and due to their geometry, are associated with the EFS and /or EDFS; hence some of the observed seismicity may have nucleated along these secondary faults (Fig. 4). The depth cross-sections also highlight the fact that the swarm initiated in June–December 2021 along the EF, while during January–August 2022 the activity migrated to EDFS. Another interesting observation is that most of the earthquakes are located between depths of 6–14 km and they lie within the hanging-wall of these fault systems. The shallow cutoff depth of ~6 km agrees well with the transition depth from creep to seismic rupture in carbonate rocks as observed in laboratory experiments and earthquake locations in areas where such rocks occur (Passelégue et al., 2019 and references therein). In an effort to check whether we can obtain sharper images of the seismicity we also calculated relative locations using the double-difference algorithm (Waldhauser and Ellsworth, 2000) and employed the P-wave minimum 1D model with a Vp/Vs ratio of 1.69 (average Vp/Vs for the top 20 km of the minimum 1D model). Figure S4 in the Supporting Information shows the same depth cross-sections for the relative locations where it can be seen that the seismicity distribution is very similar, thus we opted for utilizing the NonLinLoc locations in the subsequent analysis.

3.2. *Analysis of seismicity migration*

Pore pressure diffusion is a process that is commonly utilized in order to explain the spread of seismicity during earthquake swarms and suggests that the distance of the propagating pore pressure front should follow a parabolic profile as a function of time (Shapiro et al., 1997; Parotidis et al., 2003). In order to check whether this is the case for the Thiva swarm we included in the analysis all the earthquakes with location uncertainties less than 1.0 km. The diffusion origin was optimized via grid search at a spacing of 100 m around the centroid of the earliest events, rather than assuming the location of the first event as the origin. For each origin point we estimated the linear regression of time t versus $r^2/4\pi$, where r signifies Euclidean distance of each event from the origin point and the slope of this line represents the diffusion coefficient D. The optimal origin point was then selected as the one that maximized the coefficient of determination R^2 for the regression. This procedure yielded a diffusion origin point with coordinates 38.3444°, 23.3080° which lies to the northwestern edge of the swarm (Fig. 6a) and a diffusion coefficient of 0.238 m^2/s, however, R^2 was found to be only 0.08 and the resulting envelope fit quite poor (Fig. 6b). One plausible reason for this poor fit may be that the location uncertainty is still high, therefore we chose to perform a Monte Carlo simulation in order to ascertain what is the contribution of this factor to the diffusion model fitting. For this purpose we created 5000 datasets consisting of events with locations that are perturbed by adding a random number drawn from a normal distribution with mean and standard deviation equal to those of the horizontal uncertainties (0.92 ± 0.56 km). For each of these datasets the regression was performed and the diffusion coefficient was calculated as the slope of the line. The mean value of the diffusion coefficient for the 5000 datasets was 0.249 m^2/s which is very close to our original estimate (Fig. 6c). Furthermore we find that the slope variance due to the location uncertainties is ~19.4% much smaller than the variance of the assumed diffusion model (~80.6% Fig. 6d). These results did not change even when we partitioned the data into different time periods and point to the possibility that pore pressure diffusion may not be the primary mechanism that controlled the seismicity evolution during the swarm.

To better understand the evolution of swarm activity over time, we again divided the events into distinct phases based on the spatiotemporal clustering observed previously (see Section 3.1): Phase 1 (June to December 2021), Phase 2 (January to August 2022), and Phase 3 (September 2022 onward). For each phase, we first determined the main direction of the fault by using Principal Component Analysis (PCA). We then refined this direction by testing small adjustments (±10°) to find the direction that gave the strongest linear relationship between distance along the fault and time. To check for linear migration we fitted distance along strike versus time, where the slope of this line gives the migration rate in km/day and also calculated the coefficient of determination. To assess if the rate is statistically meaningful, we computed the p-value using a t-test, which tests whether the slope is significantly different from zero. We additionally used a

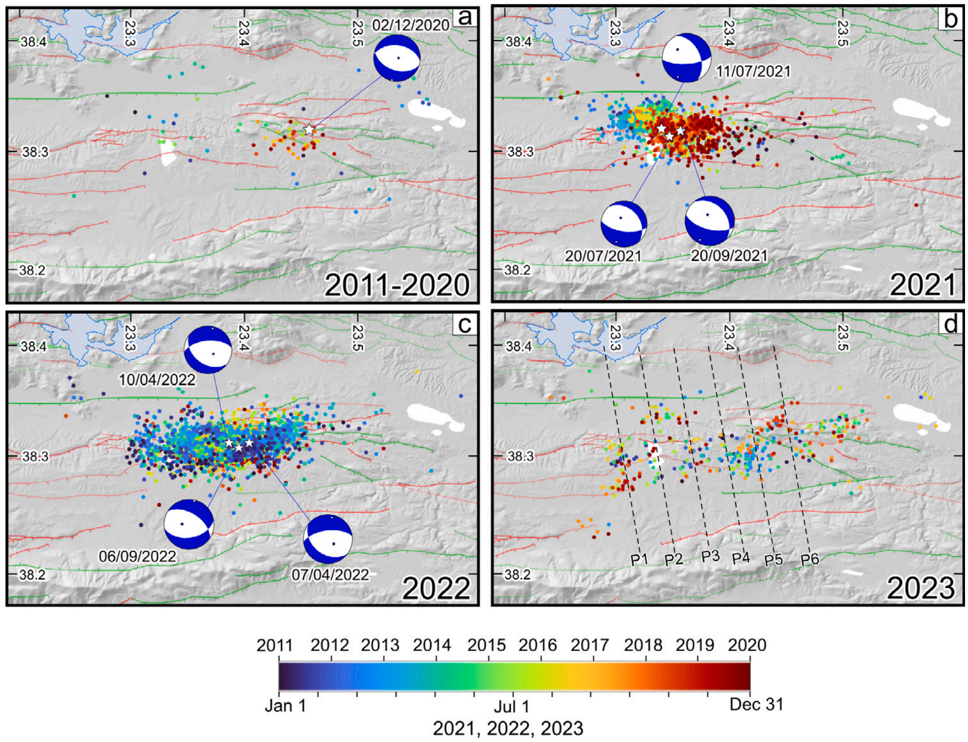

Fig. 4. DEMs with overlain hillshades (a)–(d) showing the temporal evolution of seismicity with respect to the mapped active faults for the different time periods considered in this work. NonLinLoc earthquake locations included on these maps have horizontal uncertainties of less than 1.0 km. The beachballs represent the source mechanisms of the moderate (Mw 3.9–4.6) events that occurred during 2020–2023 and were adopted from NOAIG routine moment tensor database. Faults are color-coded as per legend of Fig. 1. The dashed lines on the last map give the location of profiles along which depth cross-sections were constructed and presented in Fig. 5.

Table 1
Summary of results concerning the migration of seismicity during the Thiva swarm.

Period	Rate (km/day)	CI lower	CI upper	R^2	p(t-test)	p(null)
Jun–Dec 2021	0.0337	0.0310	0.0362	0.2782	3.3e−16	0.0
Jan–Aug 2022	−0.0129	−0.0196	−0.0063	0.0112	1.84e−14	0.0
Sep 2022–2023	−0.0093	−0.0139	−0.0053	0.0052	1.58e−8	0.09

CI indicates the 95% confidence interval for the slope representing the migration speed. R^2 is the adjusted coefficient of determination once sample size is taken into account, p(t-test) is the *p*-value of the t-test for the slope, while p(null) is the *p*-value for the null hypothesis that the slope is the result of random perturbations in the data. Note that positive and negative values of migration rate signify opposite directions along the strike of the fault.

bootstrap approach (resampling the data 1000 times with replacement) to estimate 95% confidence intervals for the slope. Finally, in order to test our results against randomness a 'null model' was created by shuffling the event times randomly 1000 times recomputing R^2 each time. An empirical *p*-value expressing the fraction of data where the shuffled R^2 matched or exceeded the observed was then calculated. Regression results for the three time periods are shown in Fig. 7 and all the estimated quantities are summarized in Table 1.

During June–December 2021 events showed a clear migration along the fault at a rate of 0.0337 km/day, meaning that the seismicity front moved by about 6 km in a period of 6 months (Fig. 7a). The fit explained about 27% of the data variation with a highly significant *p*-value of 3.33×10^{-16} and an empirical *p*-value of zero (i.e none of the 1000 randomly shuffled datasets matched or exceeded this fit strength). During January–August 2022 slow migration at −0.0129 km/day is observed, however, the fit is weak explaining only 0.1% of variation, even though the slope is statistically significant (1.84×10^{-14}, empirical *p*-value of zero). The plot shows subtle clustering without strong migration in a particular direction (Fig. 7b). In the period from August 2022 onwards, the rate was −0.0093 km/day still significantly different from zero (*p*-value = 1.58×10^{-8}), but yielding an empirical *p*-value of 0.09 (>0.05) that cannot reject the null hypothesis that the slope is the result of random perturbations in the data. This is confirmed by looking at the scatter-dominated plot that indicates no clear migration pattern (Fig. 7c). Overall, the results suggest that aseismic slip and subsequent stress transfer initiated by fluids (e.g., Danré et al., 2022) as a plausible cause for the seismicity during June–December 2021, and to some extent also during January–August 2022. From that point onwards seismicity becomes sparse and its origins may be related to other mechanisms such as stress relaxation.

4. Temporal variation of seismicity properties

4.1. Cumulative seismic moment and effective stress drop

The cumulative seismic moment that was released during the Thiva swarm is an essential parameter if one wants to investigate further the effective stress drop of earthquake clusters at the two activated faults. Before we calculate seismic moment, the local magnitudes (M_L) contained in the NOAIG catalog have to be converted into equivalent

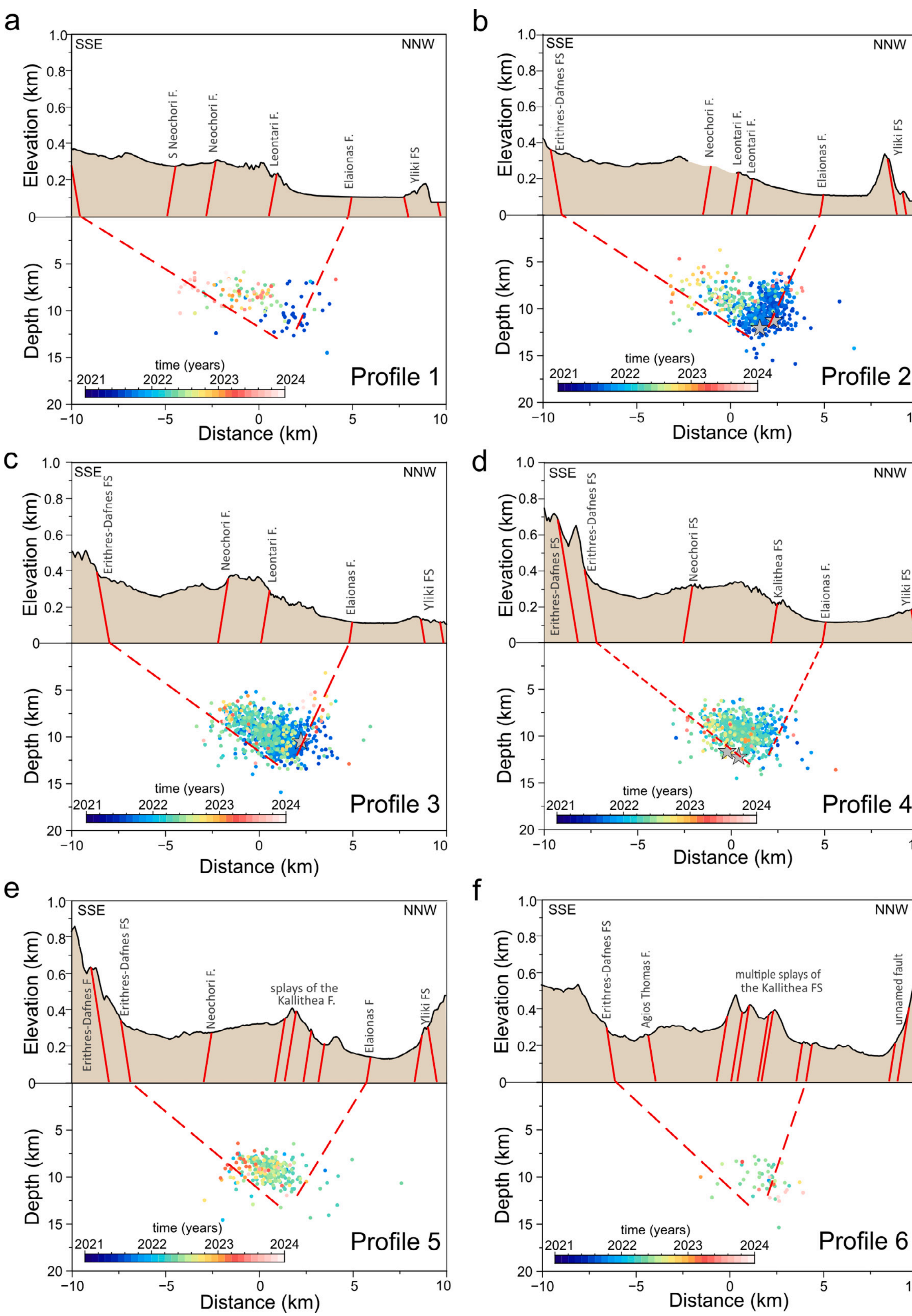

Fig. 5. Depth cross-sections (a)–(f) along the 6 profiles that are shown in Fig. 4d for 2021–2023. On top of each cross-section there is the corresponding topographic profile highlighting relationships between observed seismicity at depth and active fault traces at the ground surface. Fault dip is averaged from field measurements and includes uncertainties of ±20°. Dashed red lines indicate the projected fault dip at depth on the EDFS and EF. Note that the bulk of seismicity is 'enclosed' within the graben defined by the N-dipping EDFS and the S-dipping EF. The gray stars indicate the NonLinLoc locations of the moderate events (Mw 3.9–4.3) that occurred during the swarm.

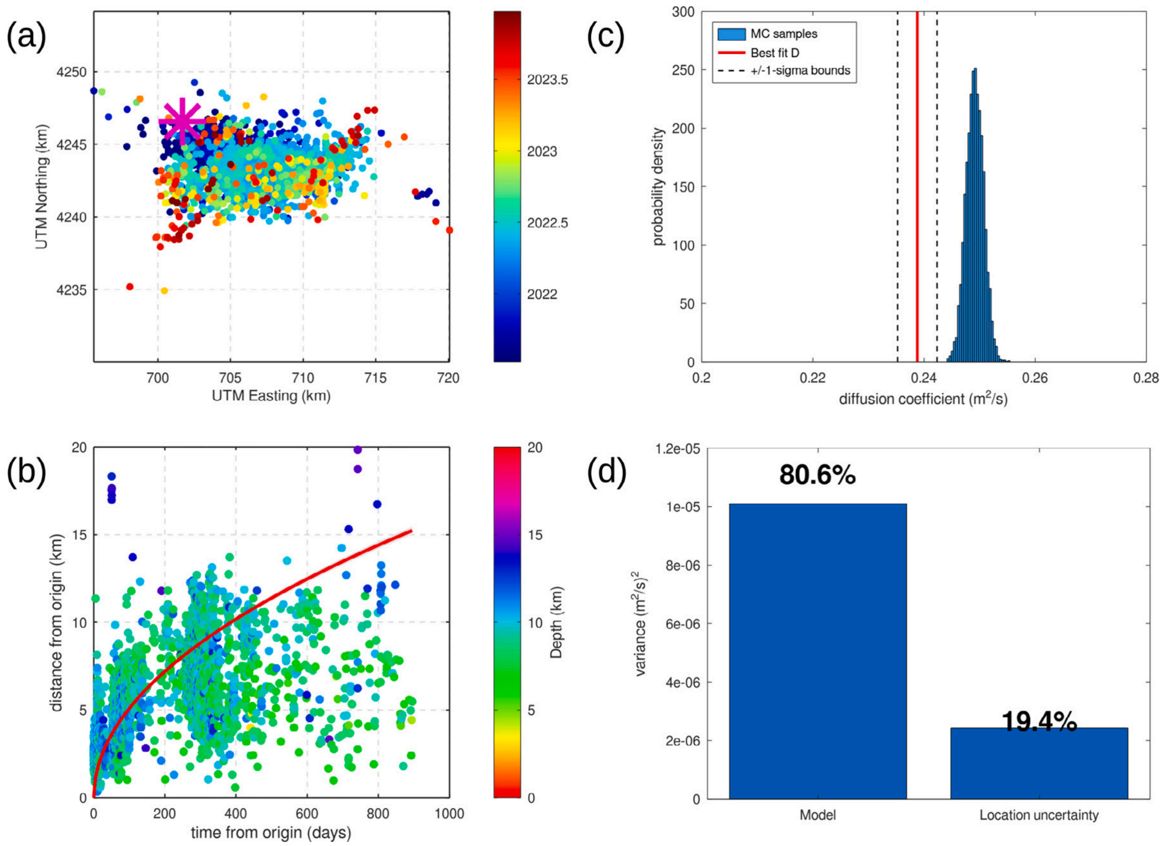

Fig. 6. Summary of analysis for the calculation of the diffusion coefficient: (a) Map (in UTM coordinates) of the 2021–2023 swarm where the large magenta star shows the best-fit origin point of the diffusion, (b) Diagram of $r^2/4\pi$ versus time utilized for estimating the diffusion coefficient. The red curve represents the parabolic profile corresponding to a diffusion coefficient of 0.23 m^2/s with $R^2 = 0.08$ (see text for more details), (c) Histogram showing the distribution of the diffusion coefficient derived after perturbing event locations for 5000 times; the red line highlights the diffusion coefficient value corresponding to the curve in panel (b) and dashed lines represent error bars, (d) Contributions of model and event location uncertainty to the total uncertainty in the estimated value of the diffusion coefficient.

moment magnitudes (Mw^*) in order to reduce uncertainties in seismic moment estimation. For events with $M_L < 3.0$ local magnitude underestimates Mw and for this range the following conversion relationship was employed (see (Deichmann, 2017) and references therein)

$$Mw^* = \frac{2}{3} M_L + 1.0 \tag{1}$$

For events with $M_L \geq 3.0$ we utilized an empirical relationship that was calibrated using HUSN-derived local and moment magnitudes through orthogonal regression (Konstantinou and Melis, 2018)

$$Mw^* = 0.991 M_L + 0.06 \tag{2}$$

Once M_L is converted to Mw^* it is possible to estimate seismic moment (in N-m) for each event and then perform a summation to obtain the cumulative value. The completeness magnitude for the period under study was found to be between 1.9 and 1.7 (see Section 4.2), hence it is unlikely that larger events are missing from the catalog. Fig. 8 shows the temporal variation of cumulative seismic moment ΣM_0 per year from 2020 up to 2023 and compares it with that obtained for the period 2011–2019. During the largest part of 2020 ΣM_0 is below 10^{14} N-m, until the December mainshock that produces a step increase to about 8×10^{15} N-m. The cumulative seismic moment history for the years 2021 and 2022 looks different since the moderate events that contribute more to ΣM_0 occurred at different times in these two years, however, the final value of ΣM_0 is very similar ($\sim 10^{16}$ N-m). In 2023 all variation in ΣM_0 occurs during the first 1.5 months attaining an almost constant value hereafter ($\sim 10^{15}$ N-m) that is one order of magnitude less than the seismic moment released in either 2021 or 2022. The year 2023 therefore can be considered as the period when swarm activity slowly ceases, since the cumulative moment that was released is very close to that prior to the increase in seismic activity (2011–2019).

Effective stress drop is a quantity utilized in cases of swarm seismicity as it can provide a measure of stress drop for a cluster of earthquakes by using the size of the activated area and the cumulative seismic moment of the sequence (Hainzl and Fischer, 2002). It can be formally defined as

$$\Delta\tau_{eff} = \frac{7}{16} \frac{\Sigma M_0}{R_A^3} \tag{3}$$

where $\Delta\tau_{eff}$ denotes the effective stress drop, and R_A is the radius of the rupture area. If the rupture area A can be approximated as circular, then its radius is given by

$$R_A = \sqrt{\frac{A}{\pi}} \tag{4}$$

We calculated the effective stress drop for the years 2021 and 2022 taking advantage of the fact that the seismicity is clustered at particular faults (EF in 2021, EDFS in 2022). We follow the methodology of Fischer and Hainzl (2017) to calculate the rupture area by using singular value decomposition in order to project the hypocenters to the plane defined by the two largest eigenvalues. The centroid of the projected hypocenters is then determined and the distance of each hypocenter from the centroid is calculated. We then estimated the median absolute deviation of all the distances and excluded any hypocenter whose distance is larger than 4.5 times this value, thus removing any potential outliers. We then applied the convex envelope algorithm in order to determine the smallest area A that contains the hypocenter projections.

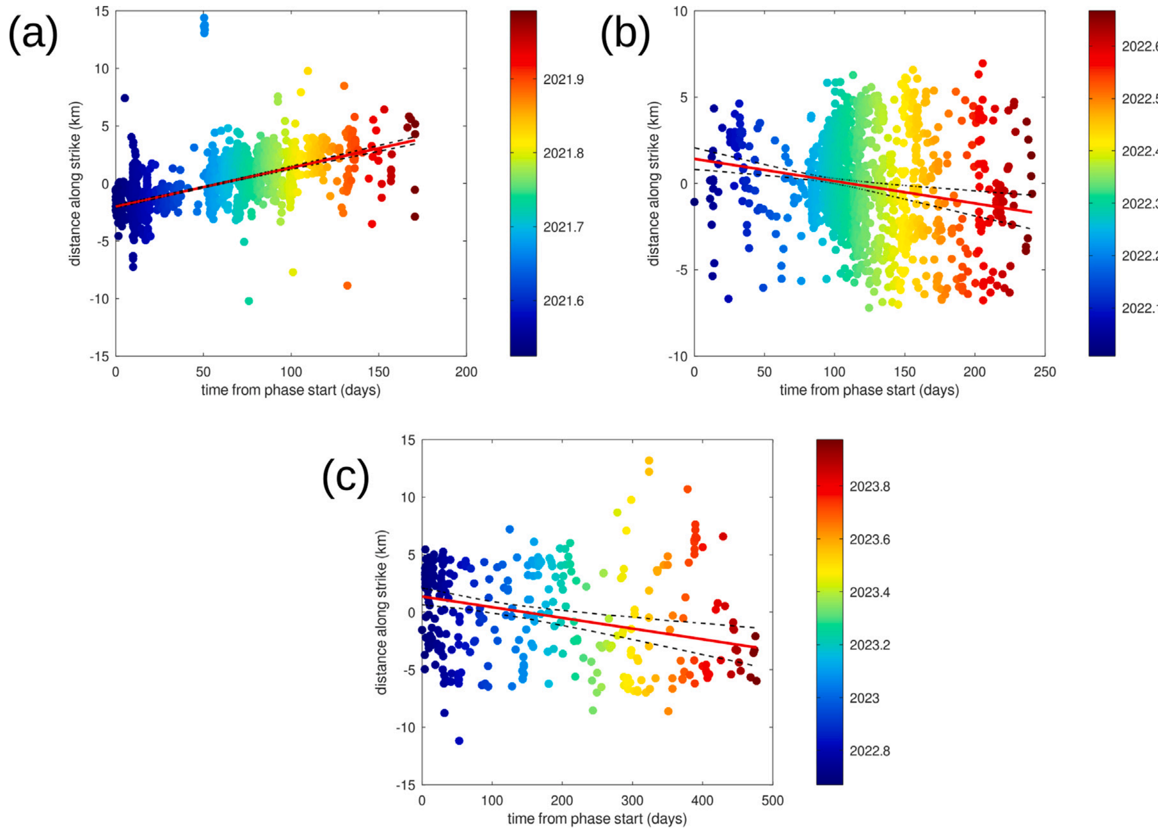

Fig. 7. Results of migration analysis of seismicity during the Thiva swarm as a function of time: (a) June–December 2021, (b) January–August 2022, and (c) September 2022 until the end of 2023. The red line shows the best fitting line and the black dashed lines represent the 95% confidence intervals (see text for more details). Projected earthquake locations are colored based on their origin time given by the scale at the right of each diagram.

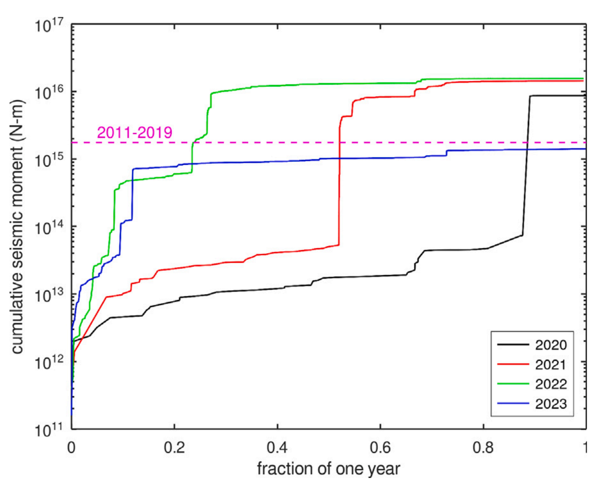

Fig. 8. Evolution of cumulative seismic moment per year during the period 2020–2023 and its comparison with the value obtained for the years 2011–2019 shown as dashed line. The time axis is normalized to represent fractions of one year.

This algorithm is implemented in function *convhull* which is freely available in GNU Octave.

Table 2 provides a summary of all the quantities related to the effective stress drop calculation for each of the three years considered. As it can be seen the size of the rupture area varies very little in 2021 and 2022 (28.9–27 km^2). The cumulative seismic moment also changes very little after removing the outliers and is almost the same per year as determined earlier. Unavoidably, there is only a slight variation in the effective stress drop in 2021 and 2022 (from 0.22 MPa to 0.25 MPa). The estimates of $\Delta\tau_{eff}$ for 2021–2022 fall within the lower end of effective stress drop estimates (0.1–3 MPa) for natural and induced swarms (Fischer and Hainzl, 2017). At this point we would like to note that if the true rupture radius is 80% of the observed value (due to location scatter artificially inflating the distribution), the effective stress drop would increase by a factor of about 1.95 (i.e. from 0.22 MPa to 0.43 MPa for 2021, and from 0.25 MPa to 0.49 MPa for 2022). However, these values still fall within, and near the lower end of the reference range specified by Fischer and Hainzl (2017). These results can be considered as another indication that aseismic slip may have played a significant role during the initiation and evolution of the Thiva swarm. Such an interpretation can be further supported by the observed differences (~0.5 units, see Table 2) between moment magnitudes calculated using ΣM_0 and those calculated from rupture area by using the relationship Mw = $\log A +$ 3.82 derived for the Mediterranean region by Konstantinou (2014).

Table 2
Summary of results concerning the temporal variation of quantities related to the effective stress drop per year.

Quantity	2021	2022
A (km^2)	28.9	27.0
R_A (km)	3.03	2.93
ΣM_0 (N-m)	1.42e16	1.48e16
$\Delta\tau_{eff}$ (MPa)	**0.22**	**0.25**
Mw(ΣM_0)	4.7	4.7
Mw(A)	5.2	5.2

The symbol ΣM_0 indicates cumulative seismic moment, Mw(ΣM_0) denotes moment magnitude calculated based on cumulative seismic moment release, while Mw(A) is moment magnitude calculated from rupture area estimates (see text for more details).

4.2. Completeness magnitude and b-value

A parameter that is frequently used in the analysis of swarm seismicity is the slope of the Gutenberg–Richter (or Ishimoto–Iida) law, more commonly referred to as the b-value (Ishimoto and Iida, 1939; Gutenberg and Richter, 1944). The b-value can be considered as a metric of the relative proportion between larger and smaller events in an earthquake population and has been found to be influenced by changes in stress, material heterogeneity, pore fluid pressure, and thermal gradients (Schorlemmer et al., 2005; El-Isa and Eaton, 2014; Scholz, 2015). The b-value can be calculated by applying the method of maximum likelihood, thus obtaining the Aki–Utsu equation (Aki, 1965; Utsu, 1965)

$$b = \frac{\log e}{< M > -(M_c - \delta M/2)} \tag{5}$$

where e is the base of natural logarithms, $< M >$ is the mean magnitude, M_c is the completeness magnitude of the catalog and δM is the amount of binning which is equal to 0.1 units for catalogs in the instrumental era. Even though the calculation of b-values looks straightforward, there are several crucial details that may lead to biased results especially when investigating temporal variations of this parameter. Marzocchi et al. (2019) identified three main issues that can affect the temporal variation of b-values: (i) the completeness magnitude and whether it changes as a function of time, (ii) the number of events above M_c, and (iii) the difference between the highest and lowest magnitude (hereafter referred to as magnitude bandwidth) in the earthquake sample. Assuming a constant M_c through time, small number of events (< 100) above M_c, or small magnitude bandwidths (< 2.0) may bias the results, leading to b-value variations that represent artifacts rather than true variations (see Marzocchi et al., 2019; Geffers et al., 2022).

We reconstructed the temporal evolution of the completeness magnitude M_c and b-value for the Thiva swarm during 2021–2023 by using the Aki–Utsu equation and performing the calculations for a sliding window moving at a step of one event at a time. The size of the window (i.e number of events it contains) was determined using the Magnitude Bandwidth Criterion which finds the window size that maximizes the number of windows with magnitude bandwidth of 2.0 or higher (for more details see (Konstantinou, 2022)). Unfortunately this maximization occurs in our case when the window is equal to 1790 events (95% of windows have magnitude bandwidth ≥ 2.0), leading to an overly smoothed and shrinked b-value time series (see Fig S5 in the Supporting Information). Therefore we choose a window size of 1000 events (70% of windows have magnitude bandwidth ≥ 2.0) which was found to preserve the b-value variations and ensures that all windows contain more than 100 events above M_c. For each of these windows M_c was estimated using the maximum curvature method after applying the correction suggested by Woessner and Wiemer (2005). In order to preserve the principle of causality the calculated b-value was placed at the time of occurrsence of the last event in each of the windows. Uncertainties for M_c and b-values are assessed by creating 200 bootstrap samples for each window and by taking the standard error of these samples as the final uncertainty for both quantities. The temporal variation of M_c, b-values, and their uncertainties can be found in Table S4 in the Supporting Information.

The temporal evolution of the completeness magnitude shows a gradual decrease from 1.9 at the beginning of the swarm, to about 1.7 in the second half of 2022 and until the end of 2023 (Fig. 9). This agrees well with previous studies that mapped the completeness magnitude across HUSN as equal to 2.0 for central Greece (D'Alessandro et al., 2011), and by the fact that in June 2021 temporary stations were installed that increased the detection capability of the network. The b-value itself exhibits a gradual increase from 1.0 in early June 2021 to a maximum value of 1.4 in February of 2022 followed by a sudden decrease to 0.9 in March 2022. The b-value starts increasing again to about 1.4 in late April 2022 and then exhibits a long-term decrease to 1.1 towards the end of 2023. These observations can be interpreted in two ways, namely in terms of stress loading and also in terms of the geometrical properties of the seismicity distribution. The first interpretation has to do with the sudden decrease of the b-value in early 2022 which may be attributed to an increase of stress loading (Scholz, 2015) in the area of the swarm, probably due to the fluid overpressure. The second one is based on the relationship of the fractal dimension D_f of the seismicity distribution with the b-value which is $D_f = 2b$ (Turcotte, 2012). The fractal dimension starts in June 2021 very close to 2.0 indicating that seismicity focused on the plane of EF and increased to 2.8 (2 × 1.4) in late 2021 as the earthquake hypocenters spread to the 3D rock volume of the hanging-wall. The opposite process occurred in early 2022 when D_f dropped to 1.8 (2 × 0.9) with seismicity localizing along the plane of EDFS. However, D_f increased again to 2.8 by late April 2022 as the earthquakes started spreading to the hanging-wall of EDFS. The fractal dimension eventually dropped to ~2.2 (2 × 1.1) indicating that towards the end of the swarm, hypocenters were nucleating again near the plane of this fault (see depth cross-section in Fig. 5e).

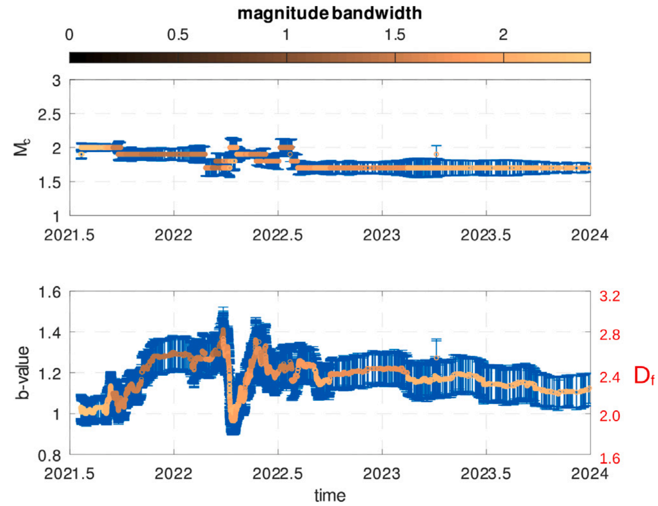

Fig. 9. Temporal variation of completeness magnitude, b-value, and fractal dimension D_f (in red) from June 2021 until the end of 2023 calculated for a window size of 1000 events. Each circle represents a time window over which the two quantities are estimated. The color of each circle follows the scale at the top and signifies the magnitude bandwidth of each window. The blue error bars indicate bootstrap uncertainties for each window.

4.3. Vp/Vs ratio and seismic velocities

As shown earlier fluid movement was probably the trigger of the Thiva swarm, hence knowledge of how the Vp/Vs ratio varies as a function of time would be beneficial in order to decipher the type of fluid involved and how rock saturation evolved. The calculation of Vp/Vs can be performed by plotting P-phase arrival times versus the difference of S-P times and finding the slope of the line described by Wadati (1933)

$$\frac{Ts - Tp}{Tp} = \frac{Vp}{Vs} - 1 \tag{6}$$

where Ts and Tp are the P- and S-wave times respectively. We take advantage of the fact that the six temporary stations lie almost directly above the area of the swarm (see Fig. 1) and use their P-phase and S-P differential times in order to perform a least-squares regression. The Vp/Vs ratio was then obtained for a sliding window of 30 days, starting the calculation in June 2021 up to the end of 2023. For the purpose of minimizing data scatter and reducing as much as possible

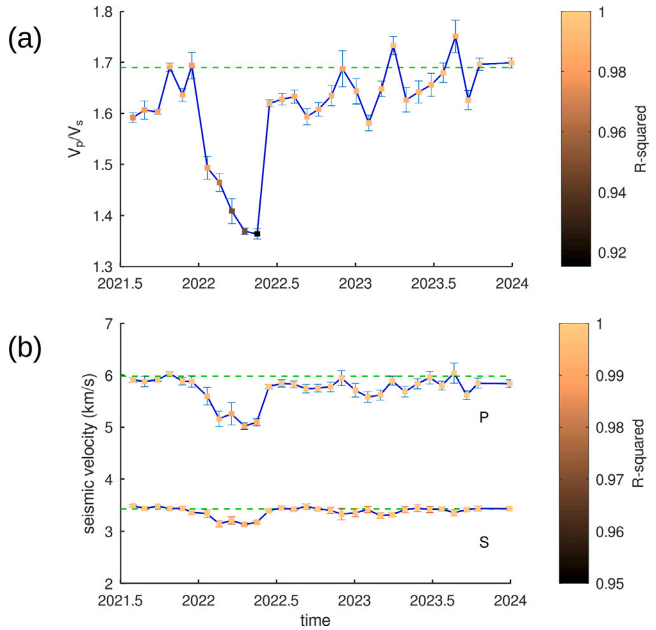

Fig. 10. (a) Variation of Vp/Vs ratio as a function of time estimated for a sliding window of 30 days, and (b) the same for the seismic velocities. The color of each square indicates the R^2 value of the regression in the final iteration. The green dashed lines represent the average Vp/Vs, Vp, Vs obtained for the top 20 km of the minimum 1D model shown in Fig. 3. The error bars in both diagrams represent the 2σ uncertainty of the slope in each regression.

the uncertainties, we followed the approach of Jo and Hong (2013) where the regression is performed in iterations. In each iteration the best-fitting line is determined, the residuals of all data points are calculated, and data points with residuals that fall outside one standard deviation of the mean are excluded. The iterations stop when the standard error of estimate decreases to 25% of its initial value. The value of 25% is a compromise between setting a higher threshold that would retain more scatter, and lowering the threshold below 25% that would result in some of the windows containing less than 30 data points. For all windows the coefficient of determination is high ($R^2 \geq 0.92$) and the 2σ uncertainty of the slope remains low (Tables S5-S7 in the Supporting Information). Examples of Wadati plots comparing data from three different periods can be found in the supporting information (Fig. S6).

Fig. 10a shows the temporal variation obtained for the Vp/Vs ratio along with the average Vp/Vs (~1.69) determined for the top 20 km of the minimum 1D velocity model (see Fig. 3) shown as a dashed line. At the beginning of the swarm Vp/Vs has a rather low value of 1.60 which towards the end of 2021 fluctuates between 1.65–1.70; however, during the first months of 2022 a steep decline occurs reaching a minimum of 1.36 in March-April 2022. After this the Vp/Vs ratio recovers to its initial value of 1.60 within 30 days and it is exhibiting an increasing but fluctuating trend towards ~1.70 until the end of 2023. When compared to the average Vp/Vs, the value of 1.36 represents a remarkable decrease of about 24% and also coincides with the decrease of the b-value at the same period as described previously. In order to investigate further the origin of this decrease we also calculated how the Vp and Vs velocities varied in the same period. For this calculation we used the P- and S-phase times from the six temporary stations versus the corresponding ray lengths, estimated by assuming straight raypaths from source to receiver. An iterative least-squares regression is applied in the same way as before for determining Vp and Vs velocities as a function of time (Fig. 10b). When compared to the average P and S velocities (5.98 km/s, and 3.43 km/s respectively) of the minimum 1D model, both Vp and Vs exhibit a decrease during the first months of 2022. However, the decrease is more severe for Vp (~20%) than the corresponding decrease of Vs (~11%). It is also important to notice that except from the early months of 2022, Vs largely coincides with the average S velocity, in contrast to Vp that remains below 5.98 km/s almost for the entire period of study. Examples of P, S-phase travel times versus raylength comparing data from three different time periods can be found in the supporting information (Fig. S7-S8).

It is possible to use Gassmann's equations in order to calculate theoretical Vp/Vs ratios for different fluid types and compare them to the observations. The velocity form of these equations can be written as (Mavko et al., 2009)

$$\frac{Vp}{Vs} = \sqrt{\frac{K_{dry}}{G} + \frac{4}{3} + \frac{K_p}{G}} \tag{7}$$

$$K_p = \frac{\eta^2}{\Phi/K_f + (1-\Phi)/K_s - K_{dry}/K_s^2} \tag{8}$$

$$K_{dry} = K_s(1-\eta) \tag{9}$$

where G is the bulk modulus, η is the Biot parameter, Φ is porosity, K_s and K_f are the bulk modulus of the rock skeleton and of the fluid respectively. We considered three types of fluids, namely brine (K_f = 10 GPa), H_2O (K_f = 2.2 GPa), and CO_2 (K_f = 0.2 GPa) while we assume η = 0.8, G = 30 GPa, and K_s = 45 GPa (values adopted from (Mavko et al., 2009; Dahm and Fischer, 2014)). The variation of the theoretical Vp/Vs ratio for the three types of fluids as a function of rock porosity Φ can be seen in Fig. 11. All three types of fluids produce a decrease in the Vp/Vs ratio as rock porosity increases, with brine showing the slowest decrease reaching Vp/Vs = 1.36 only for the highest porosity ($\Phi \approx 1.0$). On the other hand, H_2O reaches this value at $\Phi \approx 0.2$, while CO_2 does so at $\Phi \approx 0.018$ that represents almost one order of magnitude smaller porosity. Therefore CO_2 can explain the sharp drop in the Vp/Vs ratio by invoking a very modest increase in porosity (from 10^{-3} to 0.018) which can be easily reversed (e.g., due to mineral precipitation) leading to the rebound of Vp/Vs (~1.60–1.70) as observed after March 2022. The existence of CO_2 can also explain why the P-wave velocity drop is almost twice in amplitude compared to that of the S-wave velocity. P-wave velocity can be significantly reduced if the pores of the rock are filled with supercritical CO_2 transitioning to a gaseous phase. Such a fluid would increase the volumetric compliance of the rock (i.e compressibility β) producing a decrease in the bulk modulus K ($=1/\beta$). Since the P-wave velocity is proportional to $\sqrt{K}$, this will result in a significant reduction of Vp as shown in Fig. 10b. A similar interpretation to ours has been proposed by Dahm and Fischer (2014) in order to explain very low Vp/Vs ratios (~1.38) found at 7–10 km depth during a swarm in NW Bohemia and was also attributed to a gaseous phase saturating the porous rocks.

5. Moment tensor inversion

5.1. Data preprocessing and stability tests

Numerous small earthquakes occurred during the swarm that were recorded by the temporary and permanent stations with high signal-to-noise ratio making feasible the study of their source properties by means of moment tensor inversion. Here we use a method that inverts P-wave polarities and amplitude ratios in order to derive the full moment tensor of these earthquakes. Similar methodology was utilized previously by many studies (Miller et al., 1998; Jechumtálová and Šílený, 2005; Vavrycuk et al., 2008; Andinisari et al., 2021) therefore only a brief summary will be presented here. The method determines the full moment tensor **m** by iteratively performing minimization of the objective function

$$F = \sum_i |\mathbf{g_i^T m} - r_i| \tag{10}$$

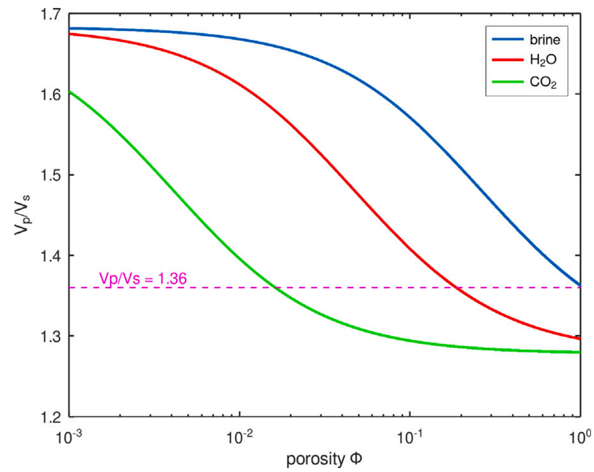

Fig. 11. Theoretical Vp/Vs as a function of porosity for three types of fluids calculated using Gassmann's equations. Dashed line shows the minimum Vp/Vs observed during the Thiva swarm.

where $\mathbf{g}$ is a column vector of six elements of the Green's function for a particular wave type (P or S), and r_i indicates the ith observed amplitude ratio. Amplitude ratios do not contain information about the sense of motion in the earthquake source, hence P-wave polarities are used as constraints in the form of inequalities such as

$$\mathbf{g}^{\mathbf{T}}\mathbf{m} \geq \mathbf{0}, \qquad \mathbf{g}^{\mathbf{T}}\mathbf{m} \leq \mathbf{0} \tag{11}$$

The use of amplitude ratios for moment tensor inversion has two advantages, namely the elimination of the need to remove the instrument response, and the significant reduction in the influence of the velocity structure since direct P and S-wave amplitudes are affected in a similar way by path effects. Two disadvantages one could mention is that this methodology is more intensive in data preprocessing than amplitude inversion, and it requires nonlinear optimization of the objective function in order to obtain a solution. We therefore used sequential quadratic programming (Nocedal and Wright, 2006) for this task which can minimize objective functions that are subjected to inequality constraints and is implemented in function *sqp* which is freely available in GNU Octave.

A search in the Thiva swarm catalog between June 2021 and December 2023 yielded 144 earthquakes with $M_L \geq 2.8$ that could potentially be used for moment tensor inversion. Setting the magnitude threshold to 2.6 would certainly increase the number of available earthquakes, however, inspection of the waveform data showed that for many of these smaller events it becomes difficult to decipher unambiguous P-wave polarities at the more distant stations. P-wave polarities were identified in the unfiltered vertical component of each station and were included in the inversion only when they exhibited an unambiguous motion of up or down. P-wave amplitudes were picked after lowpass filtering the seismograms with a corner frequency of 5 Hz in order to avoid the higher frequencies that are severely distorted by scattering. In all cases polarities remained the same before and after filtering. The horizontal components were first rotated into radial-transverse co-ordinate system with respect to the NonLinLoc location, filtered in the same way as the vertical, and SH amplitudes were picked in the transverse component. Even though in some cases SV amplitudes could be clearly seen in the radial component, we opted for not including them in our analysis since they are prone to severe distortions due to their interaction with the topography. Before forming the SH/P ratios the amplitudes were corrected for the free surface effect and for attenuation. The attenuation correction is a factor that relates the observed amplitude ratio (A_P/A_S) with the amplitude ratio that would be observed at the source (A_{P0}/A_{S0}) and it takes the form (Miller et al., 1998)

$$\frac{A_{P0}}{A_{S0}} = \frac{A_P}{A_S}\frac{R_P}{R_S}\exp\left[\pi f_c t_P^*\left(1 - \frac{Q_P}{Q_S}\right)\frac{Vp}{Vs}\right] \tag{12}$$

where R_P, R_S are geometrical spreading factors for P and S-waves, f_c is the corner frequency used for seismogram filtering, t_P^* is the whole-path attenuation operator for the P-wave, Q_P, Q_S are the quality factors of P, S-waves. In order to apply this correction we take $R_P/R_S = 1.0$, $Q_P/Q_S = 9/4$, $f_c = 5$ Hz, $t_P^* = 0.03$ s, as in a similar study of HUSN data (Andinisari et al., 2021). Since the Vp/Vs ratio changes significantly during the period of interest, we interpolated the curve of the Vp/Vs variation as a function of time (see Fig. 10a) in order to be able to use the value that is more appropriate at the occurrence time of each earthquake. Station azimuths, epicentral distances, and take-off angles for each event were derived from the corresponding absolute locations. NonLinLoc provides a quality score for the take-off angles (0: poor quality, 10: best quality), hence we utilized stations only when their take-off angles had scores between 9–10.

Each moment tensor solution was decomposed into a Double-Couple (DC), Compensated Linear Vector Dipole (CLVD), and isotropic (ISO) component whose percentages were calculated by using relative scale factors (Vavryčuk, 2015). The stability of each solution was tested in two different ways, namely by adding random noise to the observed amplitudes (noise test), as well as by removing one station at a time (jackknife test). For the noise test we added random noise to the picked amplitudes up to 20% of the maximum amplitude of each waveform and constructed 100 'noisy' datasets for each event and inverted them in the same way as the actual data. In the jackknife test we excluded one station at a time and performed the inversion again, in effect checking the stability of the moment tensor for the most critical factor which is the station distribution. We then consider a moment tensor solution as well-constrained if it conforms to the following criteria: (i) the P and T axes of the solutions produced by the two tests form similar clusters indicating a stable DC component, (ii) the sum of standard deviations of all components ($\sigma_{DC} + \sigma_{CLVD} + \sigma_{ISO}$) is less than or equal to 50% for the solutions produced in either test, and (iii) the solution is obtained by including at least 10 P-wave polarities and 4 SH/P amplitude ratios. In this way we obtained 40 full moment tensors that conformed to all three criteria and Fig. 12 shows an example of a well-constrained solution. All of these solutions and their corresponding test results can be found in the Supporting Information (Figure S9 and Table S8). It should be noted that only 2 of the moment tensors were obtained using the minimum of 10 P-wave polarities and 4 SH/P amplitude ratios, while all the rest were derived using 12–26 polarities and 6–16 ratios (see Table S8).

5.2. Results

The isotropic component of a moment tensor has a clear physical interpretation which is the occurrence of volume change (either positive or negative) at the source of the earthquake. For the well-constrained solutions of the Thiva swarm we observe isotropic components that range from −14% to 41% with 37 events having a positive isotropic component and only 3 events a negative one. These results are in accordance with moment tensors of events that occur in fluid saturated areas, such as in Jilin, NE China where isotropic components of up to 34% were observed (Zhang et al., 2019), or in the Geysers and Salton Sea areas in California where isotropic components ranged from −20% to 40% (Martinez-Garzón et al., 2017; Bentz et al., 2018). For all the solutions the sign of CLVD and ISO components is the same, precluding the possibility that the non-DC components are the results of anisotropy, since this should have produced solutions with mixed signs (Vavryčuk et al., 2008). The dominance of volume increase during the swarm can be interpreted as evidence of tensile faulting caused by high fluid pressure (Vavryčuk, 2011). Events with hypocentral depths

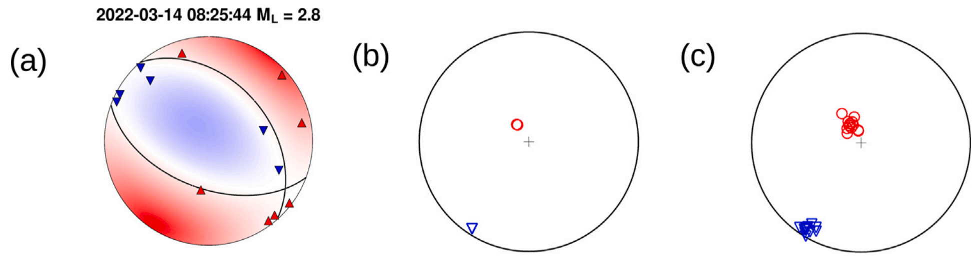

Fig. 12. Example of a well-constrained full moment tensor solution obtained after inversion of P-wave polarities and SH/P amplitude ratios. This event had a hypocentral depth of 9.8 km and its moment tensor consisted of DC = 59.4%, CLVD = 25.6%, and ISO = 15%. (a) Lower hemisphere stereographic projection of the moment tensor solution with triangles showing the stations whose P polarities were used. Blue triangles indicate dilatation and red ones compression, (b) Results of the noise test showing tight clustering of P-axes (red circles) and T-axes (blue inverted triangles), (c) The same for the results of the jackknife test.

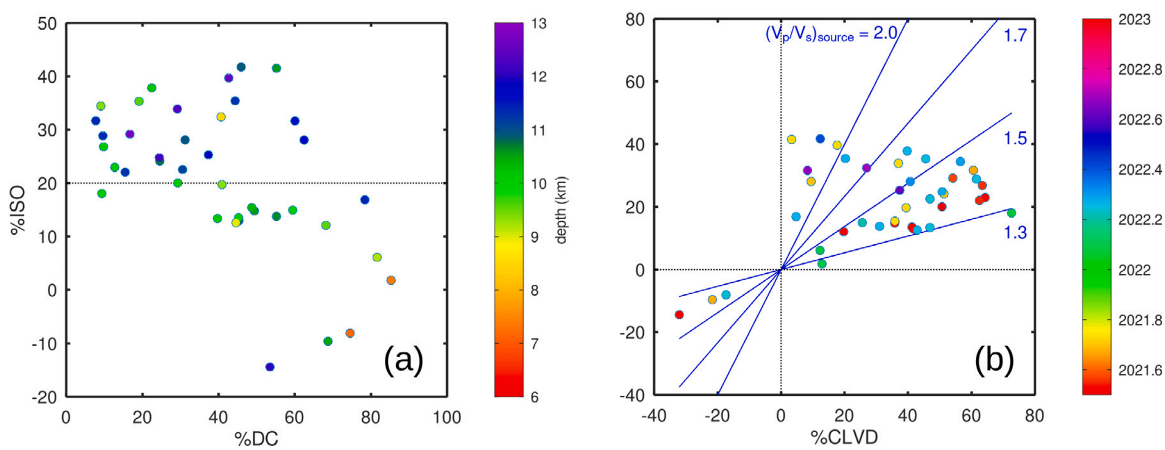

Fig. 13. Variation of moment tensor components (a) %ISO versus %DC with the color scale representing hypocentral depth, and (b) %ISO versus %CLVD with the color scale representing time of earthquake occurrence for each of the well-constrained moment tensors. The blue lines in (b) indicate the variation of %ISO and %CLVD for given values of Vp/Vs at the earthquake source (see (Vavrycuk, 2015)).

shallower than 10 km appear to exhibit large DC components (>40%) along with moderate positive or negative volume change ranging from + 20% to −14% (Fig. 13a). Positive isotropic components between 20% and 40% can be mostly found in events nucleating at greater depths (>10 km) involving a wider range of DC components (10%–65%, Fig. 13a). Therefore in both groups there are events with large positive isotropic and DC components that may represent a combined shearing and tensile faulting mechanism.

Another aspect of our results is that they can be used for inferring the Vp/Vs at the source of each earthquake, rather than an average Vp/Vs of the medium as was done in the previous section. The source Vp/Vs can be expressed as (Vavrycuk, 2015)

$$\left(\frac{Vp}{Vs}\right)_{source} = \sqrt{\frac{4}{3}\left(\frac{\%ISO}{\%CLVD}+1\right)} \tag{13}$$

where $\%ISO$ and $\%CLVD$ are the percentages of the two components. Fig. 13b shows a plot of these two components for our well-constrained solutions along with isolines of $(Vp/Vs)_{source}$ between 1.3–2.0 calculated using Eq. (13). The Vp/Vs obtained from the Wadati method (Section 4.3) represents an average value for the rocks between the earthquake sources and the stations, while $(Vp/Vs)_{source}$ given by Eq. (13) represents the Vp/Vs ratio at the source of each earthquake. The range of the two estimates generally agree (i.e the majority of them lie between 1.3–1.7), but a few deeper (> 10 km) events in Fig. 13b indicate high $(Vp/Vs)_{source}$ (they cluster around the isoline 2.0). We interpret these events as having nucleated very close to the fluid reservoir, where high fluid pressure tends to decrease the S velocity in the overlying rock thus increasing Vp/Vs (Nur, 1972). A map view of the focal mechanism solutions colored according to the percentage of isotropic component (Fig. 14) shows that the events with the largest percentage mostly occur at the center of the swarm cloud, while events that have small isotropic component (≤10%) lie at the edges. Not surprisingly, the majority of focal mechanisms exhibits pure normal faulting or a combination of normal and strike-slip faulting consistent with the stress field in central Greece (Konstantinou et al., 2017).

6. Discussion

The results presented in this work strongly suggest that the 2021–2023 Thiva swarm was caused by fluid originating from a deep (>10 km) source which likely initiated aseismic slip in the identified faults. Carbon dioxide may be the most plausible candidate fluid that is consistent with observed and theoretical estimates of Vp/Vs (Figs. 9a, 10) as well as the significant drop in P-wave velocity (Fig. 10b) that hints to the saturation of rock with a gaseous phase. However, we also need to note that to the best of our knowledge there is no direct geochemical observation of CO_2 in the Thiva area. The fluid source probably has a size of 10 km or smaller, considering the length scale of the area covered by the swarm. Unfortunately the most recent tomographic model for the Greek region (Ranjan and Konstantinou, 2024) does not indicate any significant Vp/Vs anomaly at these depths due to the fact that it can resolve anomalies only if their size is larger than 20–30 km. It is instructive then to look at other cases of swarms where high-resolution tomographic models do exist and the tectonic regime is predominantly extensional as in mainland Greece. Improta et al. (2014) obtained a Vp and Vp/Vs model for the

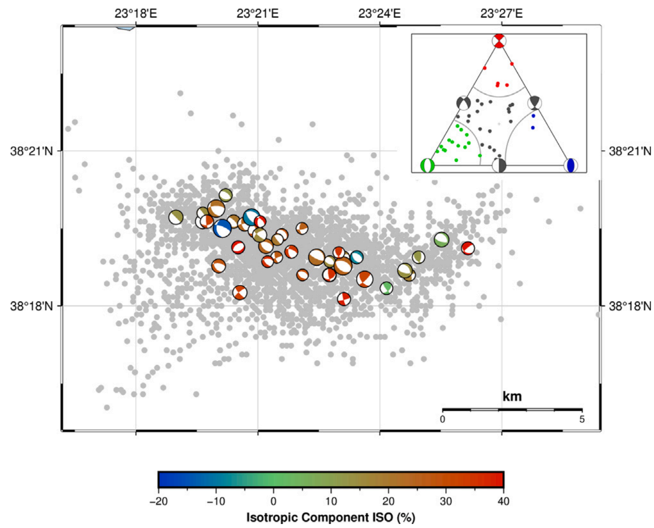

Fig. 14. Map of the study area showing the beach balls of the 40 events with a well-constrained moment tensor solution colored according to the percentage of the isotropic component. The gray dots represent NonLinLoc epicenters of the earthquakes during the 2021–2023 swarm. The inset at the upper right corner of the map represents a ternary graph describing the faulting type of the DC component for each of the well-constrained moment tensors. Green dots: pure normal faulting, red dots: pure strike-slip faulting, blue dots: pure reverse faulting, black dots: combination of two corresponding fault types.

southern Apennines in Italy, where anomalies related to fluids were detected. The authors interpreted these anomalies as localized traps of accumulated CO_2 derived from the upper mantle. The traps are formed due to the presence of an impermeable rock layer that consists of Triassic anhydrites that act as a barrier to upward fluid flow resulting in the buildup of overpressure. Large normal faults serve as conduits of the pressurized fluid triggering seismicity of variable magnitude. This process has been found to be responsible for the occurrence of large earthquakes that nucleated near the top of these traps, as for example the 1997 Umbria-Marche earthquake sequence (Mw 5.7–6.0) (Chiarabba et al., 2009) and the 2009 L'Acquila (Mw 6.1) earthquake (Baccheschi et al., 2020).

Based on the experience from the southern Apennines and the characteristics of the Thiva swarm we can reconstruct a tentative scenario describing the course of events that occurred in terms of physical processes. It is plausible to assume that a trap containing CO_2 may exist beneath Thiva at a depth greater than 10 km where at this temperature and pressure CO_2 would behave as a supercritical fluid. The source of the CO_2 may be, similar to the Apennines, the upper mantle and /or it may be the product of metamorphism of deeper carbonate rocks in central Greece. An upper mantle source is favored if one considers the existence of a low resistivity (200–400 Ohm-m) body imaged near the base of the crust beneath Thiva during a large scale Magnetotelluric survey (Galanopoulos et al., 2005). The existence of ophiolites in central Greece (Papanikolaou, 1986) offers a possible candidate for an impermeable rock type required in order to form such a trap. In terms of time, three stages of the swarm can be deciphered based on the Vp/Vs and seismic velocities variation: June 2021 until the end of the year, the first months of 2022 until the end of April, and May 2022 until the end of 2023 (see Figs. 2 and 4). Leakage of CO_2 probably started in small quantities in June 2021 as implied by the Vp/Vs value of 1.60 that may correspond to CO_2 moving into the low porosity rocks of EF. Interaction of CO_2 with water, which is likely stored in cavities inside carbonate rocks, may be responsible for the later fluctuations between 1.60–1.70 until the end of 2021. The earthquakes during this first stage must have further fractured the caprock of the CO_2 trap thus allowing larger quantities of fluid to infiltrate EDFS in early 2022, drastically decreasing the Vp/Vs ratio and the P-wave velocity. The rebound of the Vp/Vs ratio towards 1.70 that is observed in the last stage of the swarm could be the result of two processes: the escape of CO_2 towards shallower depths and its mixing with water, as well as the decrease of rock permeability after the occurrence of precipitation of minerals in the pores and cracks. The increase of permeability due to fracturing and its decrease due to mineral precipitation can affect the fluid overpressure leading to variations in seismicity rates as observed in the summer of 2021 and in early 2022. Another distinct characteristic of this swarm is that most of the seismicity is located in the hanging-wall of the activated faults (see Fig. 5). This had been observed also during the Umbria-Marche sequence and it was interpreted as a sign of significant decrease in the normal stress acting on the fault plane due to the upward diffusion of CO_2 (Miller et al., 2004). A similar process may have taken place during the Thiva swarm, and this interpretation also agrees well with the moment tensors of several events that exhibit large DC and isotropic components providing evidence for shear-tensile faulting (Fig. 13a).

The Thiva swarm was not followed by a larger earthquake as was the case in 1892–1893, and this poses the question of whether the seismic hazard in the area can be considered low at present. This question is also related to the orientation of these faults relative to the regional stress field, in the sense that unfavorably oriented faults require high pore fluid pressure in order to rupture, a condition that perhaps was not met during the 2021–2023 swarm. In a predominantly extensional regime, such as in central Greece, the reactivation angle of each fault can be estimated as 90°-δ, where fault plane dip is δ = 67°, 56° respectively. Reactivation angles are then found equal to 23° and 34°, indicating that both faults are in fact favorably oriented (Collettini and Sibson, 2001). Our attention is therefore shifted to two other parameters that play a role in the generation of large earthquakes, namely the stage of the seismic cycle of the faults and their rheology. It is well-established that large magnitude earthquakes more often occur on faults which are advanced compared to faults which are early in their seismic cycle (Kanamori and Brodsky, 2004; Scholz, 2018; Nicol et al., 2024). In Thiva, the majority of the swarm activity appears to be associated with the north-dipping EDFS, a structure that is evidenced to have accommodated numerous large events during the Holocene (Tsodoulos et al., 2008; Konstantinou et al., 2020) (Fig. 1c). The same applies for the Leontari and Kallithea south-dipping fault strands that lie immediately north of the EDFS ((Konstantinou et al., 2020); this study, Fig. 5). Hence, it is possible that the strain released along these faults over the last 10 ka reduces the likelihood of future large events on these faults (Nicol et al., 2024). In contrast, the EF where the swarm initiated, appears to have limited activity during the Holocene (Fig. 1c) and may be prone to rupture. However, one needs to consider also the rheological conditions along EF before interpreting its seismogenic potential. An inference about these rheological conditions can be gleaned from the value of the effective stress drop during 2021 (0.22 MPa). Such a low value indicates that seismicity along EF was occurring over relatively large areas, but only a small fraction of these areas was actually covered by brittle asperities (Fischer and Hainzl, 2017). This implies small isolated asperities that were embedded in a ductile rock matrix. Hence it seems that the rheology of EF may not have allowed a rupture to propagate efficiently from one asperity to the next so that it could grow in an unstable manner and produce a large earthquake.

The previous conclusion does not necessarily mean that the probability of a large event in the Thiva area is small. If the fluid is indeed carbon dioxide, then its chemical interaction with water will produce carbonic acid that can have corrosive effects on the fault rocks making them more prone to failure in the future. Ranjan and Konstantinou (2024) have found significant changes in the lithology across the fault zones of several large (Mw 6.0–6.8) earthquakes that occurred in Greece over the past 25 years. These changes are manifested as low/high P-wave velocity across the fault planes, supporting our suggestion for the weakening effect of fluids on fault rocks. Several fault traces in Thiva exhibit no Holocene scarps, while their rheological conditions are uncertain, thus they may potentially fail after being subjected to such a weakening mechanism. For example, traces of the Vilia-Skourta Fault System or the Agios Thomas Fault (Fig. 1c and Fig. 5) lie close to the swarm and they may have been affected by fluid diffusion as well. The process of rock weakening may take the form of creep, or it may manifest itself as microearthquakes with negative isotropic components as shown by Vavrycuk and Hrubcová (2017) in West Bohemia. In the former case this process can be detected by using GPS receivers, and in the latter one by routinely determining full moment tensors. The proximity of Thiva to the city of Athens raises the need for monitoring by seismic and geodetic means in order to have a realistic assessment of seismic hazard (see (Konstantinou et al., 2020)).

7. Conclusions

The main conclusions of this work can be summarized in the following points:

- The Thiva swarm involved two large normal faults of opposite dips, namely the Elaionas and Erythres-Dafnes Faults that were activated during 2021 and 2022 respectively. The migration pattern of seismicity and low effective stress drop (0.22–0.25 MPa) during 2021–2022 strongly suggests the occurrence of aseismic slip and that the asperities along the two faults were small and distributed within a ductile rock matrix. This is probably one reason why ruptures could not grow in an unstable manner resulting in a larger event.
- The temporal evolution of the Vp/Vs ratio shows a dramatic decrease during the early months of 2022 from 1.60 to 1.36 and a similar decrease can be observed for the P-wave velocities, but less so for the S-wave velocities. These observations point to a gaseous phase (such as CO_2) as the fluid that infiltrated the two faults, that also reduced the normal stress resulting in persistent hanging-wall seismicity.
- The majority of well-constrained moment tensor solutions exhibited positive isotropic components providing evidence of tensile faulting due to high fluid pressure, while some of them also exhibited large DC components that can be explained as a combination of shear-tensile faulting.
- Even though no larger earthquake followed the Thiva swarm, this does not necessarily mean that the seismic hazard in the area has decreased. The interaction of fluids with the fault rocks could lead to their weakening, and perhaps eventual shear failure in the future. If weakening takes the form of creep it can be detected by GPS receivers, while if it has a seismic expression such earthquakes would have negative isotropic components that can be determined through moment tensor inversion. Either way, it is prudent to continuously monitor this area since it is only 50 km away from Athens, the capital of Greece.

CRediT authorship contribution statement

K.I. Konstantinou: Writing – original draft, Visualization, Methodology, Formal analysis, Conceptualization. **V. Mouslopoulou:** Writing – review & editing, Validation, Investigation. **J. Begg:** Writing – review & editing, Validation, Investigation.

Declaration of competing interest

The authors declare that they have no known competing financial interests or personal relationships that could have appeared to influence the work reported in this paper.

Acknowledgments

This research has been financially supported by the National Science and Technology Council (NSTC) of Taiwan under grant NSTC 113-2116-M-008-009 awarded to the first author. Vasiliki Mouslopoulou acknowledges support from an internal National Observatory of Athens (NOA) Fellowship. The Greek Cadastre is sincerely thanked for providing access to the 2 m DEMs used for the landscape analysis. We would like to thank two anonymous reviewers, and the Editor Gregory Houseman, for their constructive comments that significantly improved our work.

Appendix A. Supplementary data

Supplementary material related to this article can be found online at https://doi.org/10.1016/j.tecto.2026.231172.

Data availability

The waveform data that were used in this study are freely available for download from National Observatory of Athens (NOA), European Integrated Data Archive (EIDA) archives under the network code Hellenic Unified Seismic Network (HUSN) (http://eida.gein.noa.gr). Initial source parameters of the earthquakes, deviatoric moment tensor solutions, and P, S arrival times are freely available in the NOAIG website (https://bbnet.gein.noa.gr). Maps were plotted using the Generic Mapping Tools package version 6.4.0 freely available from https://www.generic-mapping-tools.org/. Diagrams were plotted using functions implemented in the freely available GNU Octave (https://octave.org/). Moment tensor solutions and other stereographic projections were plotted using the MTplot package (https://github.com/djpugh/MTplot).

References

Aki, K., 1965. Maximum likelihood estimate of b in the formula $\log N$ = a–bM and its confidence limits. Bull. Earthq. Res. Inst. Tokyo Univ 43, 237–239.

Andinisari, R., Konstantinou, K.I., Ranjan, P., 2021. Moment tensor inversion of microearthquakes along the Santorini-Amorgos zone: Tensile faulting and emerging volcanism in an extensional setting. J. Volc. Geotherm. Res. 420, 107394. http://dx.doi.org/10.1016/j.jvolgeores.2021.107394.

Baccheschi, P., Gori, P. De, Villani, F., Trippetta, F., Chiarabba, C., 2020. The preparatory phase of the Mw 6.1 2009 L'Aquila (Italy) normal faulting earthquake traced by foreshock time-lapse tomography. Geology 48, 49–55. http://dx.doi.org/10.1130/G46618.1.

Begg, J.G., Mouslopoulou, V., Heron, D., et al., 2025. AFG - active faults Greece: a comprehensive geomorphology-based 1:25, 000 fault database. Sci. Data 12, 1853. http://dx.doi.org/10.1038/s41597-025-06283-z.

Bentz, S., Martinez-Garzón, P., Kwiatek, G., Bohnhoff, M., Renner, J., 2018. Sensitivity of full moment tensors to data preprocessing and inversion parameters: A case study from the salton sea geothermal field. Bull. Seismol. Soc. Am. 108, 588–603. http://dx.doi.org/10.1785/0120170203.

Cabrera, L., Poli, P., Frank, W.B., 2022. Tracking the spatio-temporal evolution of foreshocks preceding the Mw 6.1 2009 L'Acquila earthquake. J. Geophys. Res. Solid Earth e2021JB023888. http://dx.doi.org/10.1029/2021JB023888.

Chiarabba, C., Gori, P. De, Boschi, E., 2009. Pore-pressure migration along a normal-fault system resolved by time-repeated seismic tomography. Geology 37, 67–70. http://dx.doi.org/10.1130/G25220A.

Collettini, C., Sibson, R.H., 2001. Normal faults, normal friction? Geology 29 (10), 927–930.

Dahm, T., Fischer, T., 2014. Velocity ratio variations in the source region of earthquake swarms in NW bohemia obtained from arrival time double-differences. Gophys. J. Int. 196, 957–970. http://dx.doi.org/10.1093/gji/ggt410.

D'Alessandro, A., Papanastassiou, D., Baskoutas, I., 2011. Hellenic unified seismic network: An evaluation of its performance through SNES method. Geophys. J. Int. 185, 1417–1430. http://dx.doi.org/10.1111/j.1365-246X.2011.05018.x.

Daniel, G., et al., 2011. Changes in effective stress during the 2003–2004 ubaye seismic swarm. Fr. J. Geophys. Res. 116, B01309. http://dx.doi.org/10.1029/2010JB007551.

Danré, P., De Barros, L., Cappa, F., Ampuero, J.-P., 2022. Prevalence of aseismic slip linking fluid injection to natural and anthropogenic seismic swarms. J. Geophys. Res. Solid Earth 127, e2022JB025571. http://dx.doi.org/10.1029/2022JB025571.

Deichmann, N., 2017. Theoretical basis for the observed break in M_L/M_w scaling between small and large earthquakes. Bull. Seis. Soc. Am. 107, 505–520. http://dx.doi.org/10.1785/0120160318.

Derode, B., et al., 2023. Fluid-driven seismic swarms in the Gripp valley (Haute-Pyrénées, France). Geophys. J. Int. 234, 1903–1915. http://dx.doi.org/10.1093/gji/ggad175.

El-Isa, Z.H., Eaton, D.W., 2014. Spatiotemporal variations in the b-value of earthquake magnitude-frequency distributions: Classifications and causes. Tectonophys. 615-616, 1–11. http://dx.doi.org/10.1016/j.tecto.2013.12.001.

Fischer, T., Hainzl, S., 2017. Effective stress drop of earthquake clusters. Bull. Seismol. Soc. Am. 107 (5), 2247–2257. http://dx.doi.org/10.1785/0120170035.

Floyd, M.A., et al., 2010. A new velocity field for Greece: Implications for the kinematics and dynamics of the Aegean. J. Geophys. Res. 115 (B10403), http://dx.doi.org/10.1029/2009JB007040.

Galanopoulos, D., Sakkas, V., Kosmatos, D., Lagios, E., 2005. Geoelectric investigation of the hellenic subduction zone using long period magnetotelluric data. Tectonophysics 409, 73–84. http://dx.doi.org/10.1016/j.tecto.2005.08.010.

Geffers, G.-M., Main, I.G., Naylor, M., 2022. Biases in estimating *b*-values from small earthquake catalogues: how high are high *b*-values. Geophys. J. Int. 229, 1840–1855. http://dx.doi.org/10.1093/gji/ggac028.

Gutenberg, B., Richter, C., 1944. Frequency of earthquakes in California. Bull. Seismol. Soc. Am. 34, 185.

Hainzl, S., Fischer, T., 2002. Indications for a successively triggered rupture growth underlying the 2000 earthquake swarm in Vogtland/NW-bohemia. J. Geophys. Res. 107 (B12), 2338. http://dx.doi.org/10.1029/2002JB001865.

Hainzl, S., Kraft, T., Wassermann, J., Igel, H., Schmedes, E., 2006. Evidence for rainfall triggered earthquake activity. Geophys. Res. Lett. 33, L19303.

Improta, L., Gori, P. De, Chiarabba, C., 2014. New insights into crustal structure, Cenozoic magmatism, CO_2 degassing, and seismogenesis in the southern Apennines and Irpinia region from local earthquake tomography. J. Geophys. Res. Solid Earth 119, 8283–8311. http://dx.doi.org/10.1002/2013JB010890.

Ishimoto, M., Iida, K., 1939. Observations of earthquakes registered with the microseismograph constructed recently. Bull. Earthq. Res. Inst. 17, 443–478.

Jechumtálová, Z., Sílený, J., 2005. Amplitude ratios for complete moment tensor retrieval. Geophys. Res. Lett. 32 (L22303), http://dx.doi.org/10.1029/2005GL023967.

Jo, E., Hong, T.K., 2013. Vp/Vs ratios in the upper crust of the southern Korean peninsula and their correlations with seismic and geophysical properties. J. Asian Earth Sci. 66, 204–214. http://dx.doi.org/10.1016/j.jseaes.2013.01.008.

Kanamori, H., Brodsky, E.E., 2004. The physics of earthquakes. Rep. Progr. Phys. 67, 1429–1496.

Kaviris, et al., 2022. Investigation of the thiva 202–2021 earthquake sequence using seismological data and space techniques. Appl. Sci. 12, 2630. http://dx.doi.org/10.3390/app12052630.

Keranen, K., Weingarten, M., 2018. Induced seismicity. Annu. Rev. Earth Planet. Sci. 46, 149–174. http://dx.doi.org/10.1146/annurev-earth-082517-010054.

Konstantinou, K.I., 2014. Moment magnitude-rupture area scaling and stress-drop variations for earthquakes in the Mediterranean region. Bull. Seismol. Soc. Am. 104, 2378–2386. http://dx.doi.org/10.1785/0120140062.

Konstantinou, K.I., 2022. Multiyear temporal variation of b-values at Alaskan volcanoes: The synergetic influence of stress and material heterogeneity. J. Volc. Geotherm. Res. 427, 107572. http://dx.doi.org/10.1016/j.jvolgeores.2022.107572.

Konstantinou, K.I., Evangelidis, C.P., Liang, W.-T., Melis, N.S., Kalogeras, I., 2013. Seismicity, Vp/Vs and shear wave anisotropy variations during the 2011 unrest at Santorini caldera, southern Aegean. J. Volcanol. Geotherm. Res. 267, 57–67. http://dx.doi.org/10.1016/j.jvolgeores.2013.10.001.

Konstantinou, K.I., Melis, N.S., 2018. The relationship between local and moment magnitude in Greece during the period 2008–2016. PAGEOPH 175, 731–740. http://dx.doi.org/10.1007/s00024-017-1750-4.

Konstantinou, K.I., Mouslopoulou, V., Liang, W.-T., Heidbach, O., Oncken, O., Suppe, J., 2017. Present-day crustal stress field in Greece inferred from regional-scale damped inversion of earthquake focal mechanisms. J. Geophys. Res. 121, http://dx.doi.org/10.1002/2016JB013272.

Konstantinou, K.I., Mouslopoulou, V., Saltogianni, V., 2020. Seismicity and active faulting around the metropolitan area of Athens, Greece. Bull. Seism. Soc. Am. 110, 1924–1941. http://dx.doi.org/10.1785/0120200039.

Lanza, F., Roman, D.C., Power, J.A., Thurber, C.H., Hudson, T., 2022. Complex magmatic-tectonic interactions during the 2020 Makushin Volcano, Alaska, earthquake swarm. Earth Planet. Sci. Lett. 587, 117538. http://dx.doi.org/10.1016/j.epsl.2022.11.117538.

Lomax, A., Virieux, J., Volant, P., Berge-Thierry, C., 2000. Probabilistic earthquake location in 3D and layered models. In: Thurber, C.H., Rabinowitz, N. (Eds.), Advances in Seismic Event Location. Kluwer, Amsterdam, The Netherlands, pp. 101–134.

Maleki, V., Shomali, Z. Hossein, Hatami, M.R., Pakzad, M., Lomax, A., 2013. Earthquake relocation in the central Alborz region of Iran using a nonlinear probabilistic method. J. Seism. 17, 615–628. http://dx.doi.org/10.1007/s10950-012-9342-3.

Martinez-Garzón, P., Kwiatek, G., Bohnhoff, M., Dresen, G., 2017. Volumetric components in the source related to fluid injection and stress state. Geophys. Res. Lett. 44, 800–809. http://dx.doi.org/10.1002/2016GL071963.

Marzocchi, W., Spassiani, I., Stallone, A., Taroni, M., 2019. How to be fooled searching for significant variations of the b-value. Geophys. J. Int. 220, 1845–1856. http://dx.doi.org/10.1093/gji/ggz541.

Mavko, G., Mukerji, T., Dvorkin, J., 2009. The Rock Physics HandBook: Tools for Seismic Analysis of Porous Media. Cambridge University Press.

Miller, S., Collettini, C., Chiaraluce, L., Cocco, M., Barchi, M., Kraus, B.J.P., 2004. Aftershocks driven by a high-pressure CO_2 source at depth. Nature 427, 724–727.

Miller, A.D., Julian, B.R., Foulger, G.R., 1998. Three-dimensional seismic structure and moment tensors of non-double-couple earthquakes at the Hengill–Grensdalur volcanic complex, Iceland. Geophys. J. Int. 133 (2), 309–325. http://dx.doi.org/10.1046/j.1365-246X.1998.00492.x.

Mouslopoulou, V., Bocchini, G.-M., Cesca, S., Saltogianni, V., Bedford, J., Petersen, G., Gianniou, M., Oncken, O., 2020. Earthquake-swarms, slow-slip and fault-interactions at the western-end of the hellenic subduction system precede the M6.9 Zakynthos earthquake, Greece. Geochemistry, geophysics. Geosystems 21, e2020GC009243. http://dx.doi.org/10.1029/2020GC009243.

Mukuhira, Y., Uno, M., Yoshida, K., 2023. Slab-derived fluid storage in the crust elucidated by earthquake swarm. Comm. Earth Env. 3, 286. http://dx.doi.org/10.1038/s43247-022-00610-7.

Nicol, A., Mouslopoulou, V., Howell, A., Dissen, R.V., 2024. Why do large earthquakes appear to be rarely overdue for Aotearoa New Zealand faults? Seismol. Res. Lett. 95, 253–263. http://dx.doi.org/10.1785/0220230204.

Nocedal, J., Wright, S.J., 2006. Numerical Optimization, second ed. In: Springer Series in Operations Research, Springer Verlag.

Nur, A., 1972. Dilitancy, pore fluids, and premonitory variations of t_s/t_p travel times. Bull. Seismol. Soc. Am. 62, 1217–1222.

Papanikolaou, D.J., 1986. The Geology of Greece. Eptalofos Press, Athens.

Papazachos, B.C., Karakostas, V.G., Papazachos, C.B., Scordilis, E.M., 2000. The geometry of the wadati–benioff zone and lithospheric kinematics in the hellenic arc. Tectonophysics 319 (4), 275–300. http://dx.doi.org/10.1016/S0040-1951(99)00299-1.

Papazachos, B.C., Papazachou, K., 2003. The Earthquakes of Greece, Ziti ed. Thessaloniki, Greece.

Parotidis, M., Rothert, E., Shapiro, S.A., 2003. Pore-pressure diffusion: A possible triggering mechanism for the earthquake swarms 2000 in Vogtland/NW Bohemia, central Europe. Geophys. Res. Lett. 30, 2075. http://dx.doi.org/10.1029/2003GL018110.

Passarelli, L., Heryandoko, N., Cesca, S., Rivalta, E., Rasmid, Rohadi S., Dahm, T., Milkereit, C., 2018. Magmatic or not magmatic? The 2015–2016 seismic swarm at the long-dormant Jailolo Volcano, West Halmahera, Indonesia. Front. Earth Sci. 6, 79. http://dx.doi.org/10.3389/feart.2018.00079.

Passelégue, F.X., Aubrey, J., Nicolas, A., Fondriest, M., Deldicque, D., Schubnel, A., Toro, G. Di, 2019. From fault creep to slow and fast earthquakes in carbonates. Geology 47, 744–748. http://dx.doi.org/10.1130/G45868.1.

Ranjan, P., Konstantinou, K.I., 2024. Local earthquake tomography of the Aegean crust: Implications for active deformation, large earthquakes, and arc volcanism. Tectonophysics 880, 230331. http://dx.doi.org/10.1016/j.tecto.2024.230331.

Ross, Z., Cochran, E.S., Trugman, D.T., Smith, J.D., 2020. 3D fault architecture controls the dynamism of earthquake swarms. Science 368, 1357–1361. http://dx.doi.org/10.1126/science.abb0779.

Saltogianni, V., Mouslopoulou, V., Dielforder, A., Bocchini, G-M., Bedford, J., Oncken, O., 2021. Slow slip triggers the 2018 Mw 6.9 zakynthos earthquake within the weakly locked hellenic subduction system, Greece. Geochem. Geophys. Geosyst. 22, e2021GC010090. http://dx.doi.org/10.1029/2021GC010090.

Sboras, S., Ganas, A., Pavlides, S., 2010. Morphotectonic analysis of the neotectonic and active faults of Beotia (central Greece) using GIS techniques. Bull. Geol. Soc. Greece 43, 1607–1618. http://dx.doi.org/10.12681/bgsg.11335.

Scholz, C.H., 2015. On the stress dependence of the earthquake b value. Geophys. Res. Lett. 42, 1399–1402. http://dx.doi.org/10.1002/2014GL062863.

Scholz, C.H., 2018. Mechanics of Earthquakes and Faulting, third ed. Cambridge University Press, New York.

Schorlemmer, D., Wiemer, S., Wyss, M., 2005. Variations in earthquake-size distribution across different stress regimes. Nature 437, 539–542. http://dx.doi.org/10.1038/nature04094.

Shapiro, S.A., Huenges, E., Borm, G., 1997. Estimating the crust permeability from fluid-injection-induced seismic emission at the KTB site. Geophys. J. Int. 131, F15–F18.

Shiddiqi, H.A., et al., 2023. Seismicity modulation due to hydrological loading in a stable continental region: a case study from the Jektvik swarm sequence in northern Norway. Geophys. J. Int. 235, 231–246. http://dx.doi.org/10.1093/gji/ggad210.

Tsodoulos, I.M., Koukouvelas, I.K., Pavlides, S., 2008. Tectonic geomorphology of the easternmost extension of the gulf of corinth (beotia, central Greece). Tectonophysics 453, 211–232.

Turcotte, D.L., 2012. Fractals and Chaos in Geology and Geophysics, second ed. Cambridge University Press.

Utsu, T., 1965. A method for determining the value of b in a formula $\log n$ = a-bM showing the magnitude-frequency relation for earthquakes. Geophys. Bull. Hokkaido Univ. 13, 99–103.

Vavrycuk, V., 2011. Tensile earthquakes: Theory, modeling, and inversion. J. Geophys. Res. 116, B12320. http://dx.doi.org/10.1029/2011JB008770.

Vavrycuk, V., 2015. Moment tensor decompositions revisited. J. Seism. 19, 231–252. http://dx.doi.org/10.1007/s10950-014-9463-y.

Vavrycuk, V., Bohnhoff, M., Jechumtálová, Z., Kolár, P., Sílený, J., 2008. Non-double-couple mechanisms of microearthquakes induced during the 2000 injection experiment at the KTB site, Germany: a result of tensile faulting or anisotropy of a rock? Tectonophysics 456 (1–2), 74–93. http://dx.doi.org/10.1016/j.tecto.2007.08.019.

Vavrycuk, V., Hrubcová, P., 2017. Seismological evidence of fault weakening due to erosion by fluids from observations of intraplate earthquake swarms. J. Geophys. Res. Solid Earth 122, 3701–3718. http://dx.doi.org/10.1002/2017JB013958.

Wadati, K., 1933. On the travel time of earthquake waves, II. Geophys. Mag. 7, 101–111.

Waldhauser, F., Ellsworth, W.L., 2000. A double-difference earthquake location algorithm: Method and application to the northern Hayward fault, California. Bull. Seismol. Soc. Am. 90 (6), 1353–1368.

Wang, Q.-Y., Cui, X., Frank, W.B., Lu, Y., Hirose, T., Obara, K., 2024. Untangling the environmental and tectonic drivers of the noto earthquake swarm in Japan. Sci. Adv. 10, eado1469. http://dx.doi.org/10.1126/sciadv.ado.1469.

Woessner, J., Wiemer, S., 2005. Assessing the quality of earthquake catalogues: Estimating the magnitude of completeness and its uncertainty. Bull. Seismol. Soc. Am. 95, 684–698. http://dx.doi.org/10.1785/0120040007.

Yoshida, K., Hasegawa, A., 2018. Hypocenter migration and seismicity pattern change in the Yamagata-Fukushima border, NE Japan, caused by fluid movement and pore pressure variation. J. Geophys. Res. Solid Earth 123, 5000–5017. http://dx.doi.org/10.1029/2018JB015468.

Zhang, W., Lei, J., Sun, D., 2019. The 2013 and 2017 Ms 5 seismic swarms in Jilin, NE China: Fluid-triggered earthquakes? J. Geophys. Res.: Solid Earth 124, 13096–13111. http://dx.doi.org/10.1029/2019JB018649.